FABRICATION, CHARACTERIZATION AND CONTROL OF A NOVEL MAGNETORHEOLOGICAL ELASTOMER-BASED ADAPTIVE TUNED VIBRATION ABSORBER

Armin Rasooli

A Thesis

In

The Department

Of

Mechanical, Industrial and Aerospace Engineering

Presented in Partial Fulfillment of the Requirements for The Degree of

Master of Mechanical Engineering

Concordia University

Montreal, Quebec, Canada

December 2020

© Armin Rasooli, 2020

CONCORDIA UNIVERSITY
School of Graduate Studies

This is to certify that the thesis prepared

By: Armin Rasooli

Entitled: Fabrication, Characterization and Control of a Novel
            Magnetorheological Elastomer-based Adaptive Tuned Vibration Absorber

and submitted in partial fulfillment of the requirements for the degree of

Master of Mechanical Engineering

complies with the regulations of the University and meets the accepted standards with respect to originality and quality.

Signed by the final examining committee:

_____Chair
Dr. Subhash Rakheja

_____Examiner
Dr. Subhash Rakheja

_____Examiner
Dr. Lucia Tirca

_____ Thesis Supervisor
Dr. Ramin Sedaghati

Approved by   _____
            Dr. Ivan Contreras, Graduate Program Director

_____
            Dr. Mourad Debbabi, Dean
            Faculty of Engineering and Computer Science

<u>ABSTRACT</u>

FABRICATION, CHARACTERIZATION AND CONTROL OF A MAGNETORHEOLOGICAL ELASTOMER-BASED ADAPTIVE TUNED VIBRATION ABSORBER

By Armin Rasooli

Semi-active tunable vibration absorbers (SATVAs) have recently received growing interest due to their energy efficiency, simple structure and optimal performance under a wide frequency-bandwidth. SATVAs generally consist of elements with variable stiffness to allow for optimal performance under a wide frequency range compared with their passive analogues which are typically tuned at a particular frequency. Magnetorheological elastomers (MREs) are unique smart materials which can serve as the variable-stiffness elements in SATVAs. MREs are basically the solid state of the well-known magnetorheological (MR) fluids, which in contrast to MR fluids, their stiffness (storage modulus) can be continuously changed rapidly through the application of an external magnetic field.

The present research study is concerned with the modeling, fabrication and control of a novel SATVA based on MRE-filled sandwich structures. To this end, a novel five-layered beam-shape sandwich structure was designed using MREs as core layers, reinforced with thin elastic plates on top, middle and bottom. To provide for a suitable and controllable magnetic field a set of U-shaped electromagnets were also designed. A specific two-node adaptive sandwich beam element has been developed to derive the governing dynamic equations of the MRE-based sandwich beam in the finite element (FE) form. The developed finite element model of the MRE-based sandwich beam together with the developed magnetic finite element of the electromagnets have then been effectively utilized to identify the suitable design parameters for the proposed SATVA to meet the geometrical and mechanical requirements. Experimental tests have been designed to acquire the magnetic permeability and the storage modulus of the fabricated MREs required for the modeling.

Next the proposed SATVA was fabricated and subsequently tested using an electrodynamic shaker to evaluate its vibration performance and also to validate the developed FE models. The results indicate that the fabricated SATVA, provides an approximately 9% shift in the natural frequency. The validated FE models were subsequently utilized to conduct systematic sensitivity analysis to investigate the effect of different design parameters including the thickness of elastic layers and the position of electromagnets. The experimental results were also used to developed an equivalent lumped mass model for the proposed SATVA. Finally, a phased-based control strategy using the full-state adaptive Kalman filter (AKF) observer has been developed to adaptively tune the natural frequency of the absorber to the varying excitation conditions. It is expected that the present research dissertation provides an essential guidance for the future development of light-weight adaptive vibration absorbers.

Acknowledgment

I would like to express my most sincere gratitude and appreciation to my supervisor, Professor Ramin Sedaghati; for his patience and invaluable guidance along my master's program.

I would also like to extend my special vote of gratitude to Dr. Masoud Hemmatian for his invaluable suggestions and collaboration in the experiments that were conducted.

I would also like to thank my brother (Mr. Ashkan Rasouli) and also my parents (Mr. Afshin Rasooli and Mrs. Mehrnaz Banoo Ashraf Ganjouei), for their continuous encouragement, inspiration, and consistent help mentally and emotionally throughout these years.

Special thanks goes to all my close friends and office-mates at Concordia University: Mostafa asadi-khanouki, Hossein Vatandoost, Mana Mirmirani, Nader Mohseni and Hooman Zoka for their inspiration and support along my scholastic journey at Concordia University.

Table of contents

List of Figures

List of Tables

Nomenclature

A	Magnetic vector potential
b	Width of Sandwich Structure
B	Magnetic flux density
b_h	Width of host structure
b_{SH}	Forgetting factor in noise estimation
C_A	Equivalent damping coefficient of the vibration absorber
C_h	Equivalent damping of host structure
d_M	Position of electromagnets
E_h	Young modulus of host structure
$\mathbb{E}[.]$	Expected value operator
$\{f\}$	Assembled total force vector in FE formulation
F	Amplitude of host excitation force
f_A	Natural frequency of the vibration absorber system
$\underline{f_e}$	Element nodal force vector in FE formulation
$\underline{F}_k$	Process noise (disturbance) at time-step k
F_p	Vibration absorber's base force amplitude

F_{st}	Static force exerted on host structure
$f(t)$	Host excitation force
$G^{(i)}$	Shear modulus of layer i
$G'_{(i)}$	Storage modulus of layer i
$G''_{(i)}$	Loss modulus of layer i
$\mathbf{H}$	Magnetic field intensity
h_i, h_j	Thickness of layers i, j
$\underline{\underline{H}}_k$	observation matrix at time-step k
I	Electrical current
I_j	Second moment of area (per unit width) of layer j
$\mathbf{J}$	Current density
$[K^*]$	Assembled stiffness matrix in FE formulation
K_A^*	Equivalent complex stiffness of the vibration absorber system
K_A	Equivalent storage modulus of the vibration absorber system
$\underline{\underline{k}}_e$	Elemental stiffness matrix in FE formulation
K_h^*	Equivalent complex stiffness of host structure
K_h	Equivalent storage modulus of host structure
$\underline{\underline{K}}_k$	Kalman gain matrix

L	Length of sandwich beam
L_h	Length of host structure
l_e	Length of beam element
$[M]$	Assembled mass matrix in FE formulation
m_{A1}	Equivalent base lumped mass of the vibration absorber
m_{A2}	Equivalent sprung lumped mass of the vibration absorber
$\underline{\underline{M}}_e$	Elemental mass matrix in FE formulation
m_h	Equivalent sprung mass of host structure
N_e	Number of finite elements
N_n	Number of nodes in FE formulation
$\underline{N}_{ui}(x)$	Shape function vector for longitudinal displacement in layer i
$\underline{N}_w(x)$	Shape function vector for transvers displacement
$\underline{\underline{P}}_k$	Error covariance matrix at time-step k
$\underline{q}_e(t)$	Elemental degrees of freedom vector
$\underline{\underline{Q}}_k$	Noise covariance matrix at time-step k
Q_k	Nodal force on the k-th elemental degree of freedom
$\underline{q}_k$	Noise signal average at time-step k
q_e^k	k-th elemental degree of freedom

$\dot{q}_e^k$	Time derivative of the k-th elemental degree of freedom
$\underline{r}_k$	Measurement noise average at time-step k
$\underline{\underline{R}}_k$	Measurement noise covariance matrix at time-step k
t_h	Thickness of host structure
T_i, T_j	Elemental kinetic energy (per unit width) of layers i, j
T_s	Sampling time in the controller
$u^{(i)}(x, z, t)$	Longitudinal displacement field in layer i
$u_i^0(x, t)$	Longitudinal displacement of mid-layer i
$\dot{u}^{(i)}$	Longitudinal velocity field in layer i
$\underline{u}_k$	System input at time-step k
V_i, V_j	Elemental potential energy (per unit width) of layers i, j
V_p	Vibration absorber's base Velocity amplitude
$w(x, t)$	Transvers displacement field
$w_{,x}$	The transverse slope field
$\dot{w}$	Transverse velocity field
x_A	Displacement of the sprung mass of the vibration absorber
X_A	Fourier transform of the vibration absorber's sprung mass position
$\dot{x}_A$	Velocity of the sprung mass of the vibration absorber

$\bar{x}_e$	Normalized beam element longitudinal coordinate
x_h	Displacement of the sprung mass of host structure
X_h	Fourier transform of host structure's sprung mass position
$\dot{x}_h$	Velocity of the sprung mass of host structure
$\underline{X}_k$	Full system state vector at time-step k
$\underline{\hat{X}}_{k|i}$	State estimation at time k based on time i, $k \geq i$
$\underline{Y}_k$	Measurement (observation) signal at time-step k
$\underline{\underline{Y}}^k$	Set of all observations up to time k
z_i	Local transverse coordinate of layer i
$\{\delta\}$	Assembled displacement vector in FE formulation
$\{\ddot{\delta}\}$	Assembled acceleration vector in FE formulation
δ_{st}	Static tip deflection of host structure
ω	Forced excitation frequency of host structure
ω_A	Fundamental angular natural frequency of the vibration absorber
ω_{h1}	Fundamental angular natural frequency of host structure
η_A	Loss factor of the vibration absorber
η_h	Loss factor of host structure
$\varepsilon_{\bar{x}_e}^{(i)}$	Axial longitudinal strain in layer i

ξ_A	Equivalent damping ratio of the vibration absorber
ξ_h	Equivalent damping ration of host structure
γ	Controller gain
$\gamma_{xz}^{(i)}$	Shear strain in layer i
$\dot{\gamma}_{\bar{x}_e z}^{(j)}$	Shear strain rate in layer j
ρ_h	Host structure's volumetric mass density
ρ_i, ρ_j	Volumetric mass density of layers i, j
$\sigma_{\bar{x}_e}^{(i)}$	Axial stress in layer i
$\tau_{xz}^{(i)}$	Shear stress in layer i
ϕ	Phase difference between the relative position and host position
$\underline{\underline{\phi}}_{k+1,k}$	State transition matrix between consecutive time-steps
$\underline{\underline{\psi}}_{k+1,k}$	Input transition matrix between consecutive time-steps
$\underline{\underline{\Gamma}}_{k+1,k}$	Disturbance transition matrix between consecutive time-steps
μ	Magnetic permeability
$\underline{\nu}_k$	Measurement noise signal at time-step k

Chapter 1: Introduction, Literature Review and Objectives

1.1 Introduction

Passive tunable vibration absorbers (TVAs) are widely used to attenuate the unwanted vibrations in machinery and structures, thanks to their low production costs and reliable performance [1]. Passive TVAs generally consist of a mass, spring and damping elements whose parameters are determined at early stages of the design to tune the natural frequency of the absorber to the desired excitation frequency which may be very close to the main system fundamental frequency. While the passive tuned vibration absorbers are simple and reliable systems, their performance is mainly limited to a narrow frequency bandwidth around the tuned frequency. To increase the optimal working frequency bandwidth, the adaptive vibration absorbers are utilized, which generally comprise of stiffness-varying elements. A particular class of stiffness-varying materials are smart materials whose properties change upon the application of an external stimuli. One of such smart materials are Magnetorheological Elastomers (MREs) which can provide variation in their stiffness upon an external magnetic field. While simple MR-based vibration absorber configurations were extensively studied [2-4], the research on vibration absorbers based on MR sandwich structures is still very limited [5].

In this Chapter, the different sets of Vibration Absorbers are classified and summarized. Next, the Magnetorheological materials, their characteristics and MRE's benefits and the MRE fabrication methods and classifications are presented. Subsequently, different adaptive vibration absorbers incorporating MREs are reviewed in detail. The current study and its advantages in practical applications were also signified. Finally, the organization of the current thesis is described.

1.2 Vibration Absorbers

To increase the working frequency bandwidth of passive TVAs, various fully active adaptive tuned vibration absorbers (AATVAs) have been developed. AATVAs generally consist of passive TVA systems in conjunction with active actuators (such as piezoelectric and voice coil actuators), sensors and controllers. Contrary to their passive counterparts, AATVAs are able to suppress the host structures' vibrations over a wider frequency

range. However, the AATVAs require complex control systems with high implementation costs and demand high control effort and thus power requirement. Moreover, the vibration attenuation performance of AATVAs is highly dependent on the controller, and could cause instability if the controller is not properly designed [6, 7]. Semi-active adaptive tuned vibration absorbers (SATVAs) have recently received appropriate attention as they possess the reliability and fail-safe feature of passive systems while having the adaptability and performance gain of fully active system. In SATVAs, the system dynamic parameters (damping or/and stiffness) can be adaptively varied without inducing external forces by actuators as required in AATVAs. SATVAs can nearly offer similar performance as AATVAs while requiring less complex control hardware and energy consumption. Based on the mechanical design, semi-active adaptive vibration absorbers may be classified as the variable-geometry and smart material-based devices. For instance the variation in geometry of absorbers could be achieved by changing the number of helical springs [8] or the effective length of a cantilever beam [9], and the span between two spring poles [10].

The smart material-based semi-active vibration absorbers generally comprise of an oscillating mass mounted on a stiffness varying structure embedded with the smart semi-active materials. A variety of smart materials have been utilized in development of ATVAs such as shape memory alloys [11], magnetorheological materials [12, 13], and piezoelectric materials [14]. The Mechanical properties of these smart materials can vary upon an external stimulus. The mechanical properties, particularly the young modulus, of the shape memory alloys (SMAs) change with the variation in the temperature. Thus, the adaptive vibration absorbers incorporating the shape memory alloys operate based on the concepts of heat transfer. As shown in figure 1.1, the overall stiffness (thus the natural frequency) of SMA-based adaptive vibration absorbers can be changed and controlled by the temperature control mechanisms such as joule heating. The rheological properties, particularly shear modulus, of magnetorheological (MR) materials change with the variation in the magnetic field intensity. Hence, the MRE-based adaptive vibration absorbers comprise of magnetic field generation devices such as electromagnets. Figure 1.2, represents a conventional MRE-based SATVA in which the stiffness and natural frequency of the system can be varied and controlled by the controllable electrical current

2

input to the electromagnets' wirings. Piezoelectric materials are mostly used as actuators and sensors in mechanical structures. Piezoelectric materials convert the electrical signals into mechanical movements and vice-versa. Some adaptive tuned vibration absorbers based on piezoelectric materials have been developed based on electromechanical couplings in the piezo materials.
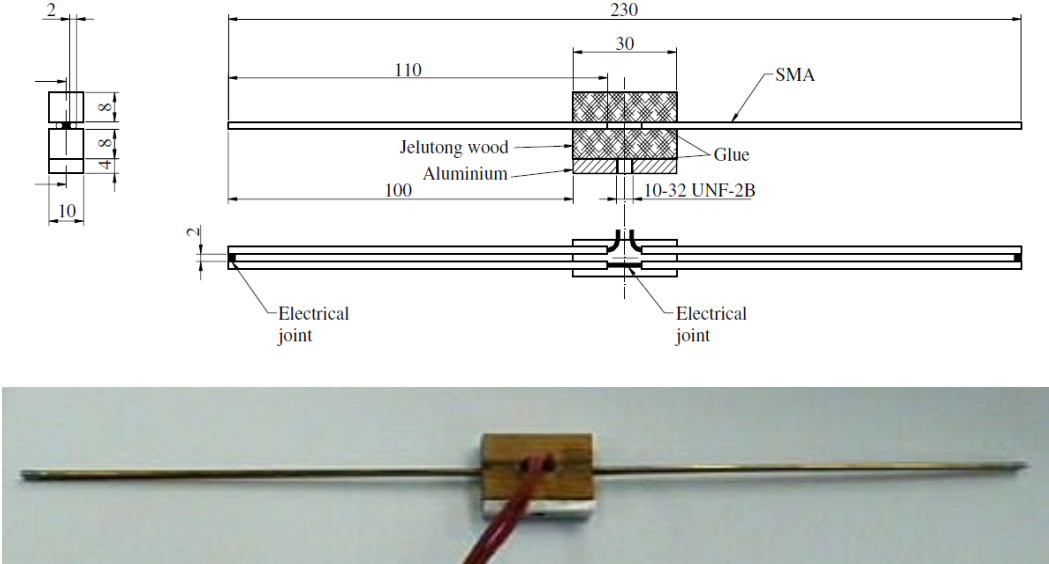
Figure 1.1 A Shape Memory Alloy (SMA) based SATVA [11]
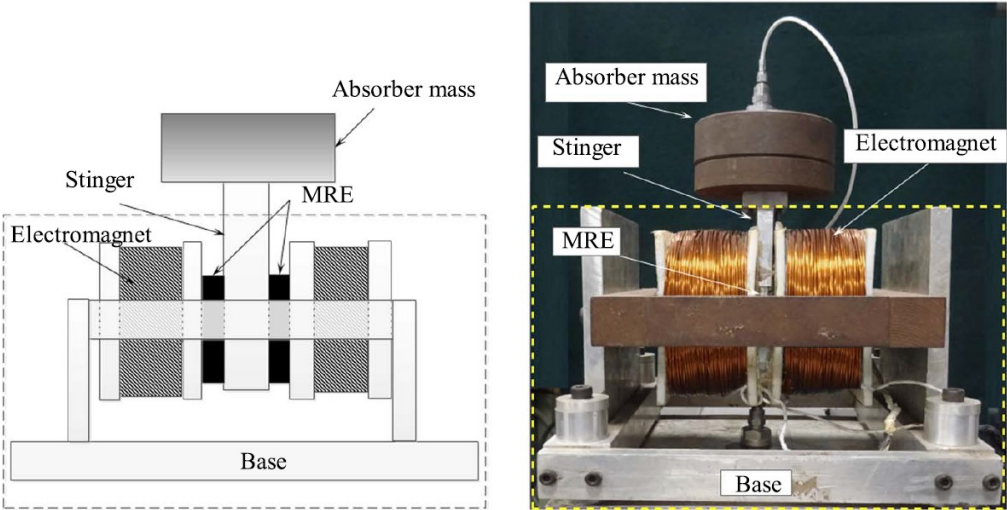
Figure 1.2 MRE-based SATVA [4]

The main purpose of all proposed SATVAs is to adaptively tune the natural frequency of SATVAs to the varying excitation frequency, thus providing the optimal vibration suppression performance [15]. Thus, the response time of the vibration suppression devices is of paramount importance. The response time associated with the magnetic field generation and control is much lower than the other stimuli control in SATVAs such as temperature control in SMA-based devices. Therefore, the MR materials are of the most suitable materials for adaptive vibration suppression systems including the SATVAs.

1.3 Magnetorheological Materials

Magnetorheological (MR) materials are a class of smart materials whose mechanical (rheological) properties can change upon application of an external magnetic field. MR materials consist of dispersed micron-sized ferromagnetic particles in a non-magnetic medium. This family of materials can be divided into three classes of MR fluids (MRFs), MR foams and MR elastomers [16]. The MR effect was first discovered by Jacob Rabinow who investigated the use of MRFs in a clutch [17].

Upon the application of a controllable magnetic field, MR materials' rheological and viscoelastic properties can be altered continuously, rapidly and reversibly which makes them ideal candidates for the development and design of novel adaptive tunable vibration absorbers (ATVAs). In the presence of an external magnetic field, the present micron-sized ferromagnetic particles will result in a higher resilience and stiffness of the overall MR material [18]. As depicted in figure 1.3, in the case of an MRF, the exerted magnetic field will result in a chain-like semi-solid structure formed by the magnetic particles which result in a higher yield strength and apparent viscosity.
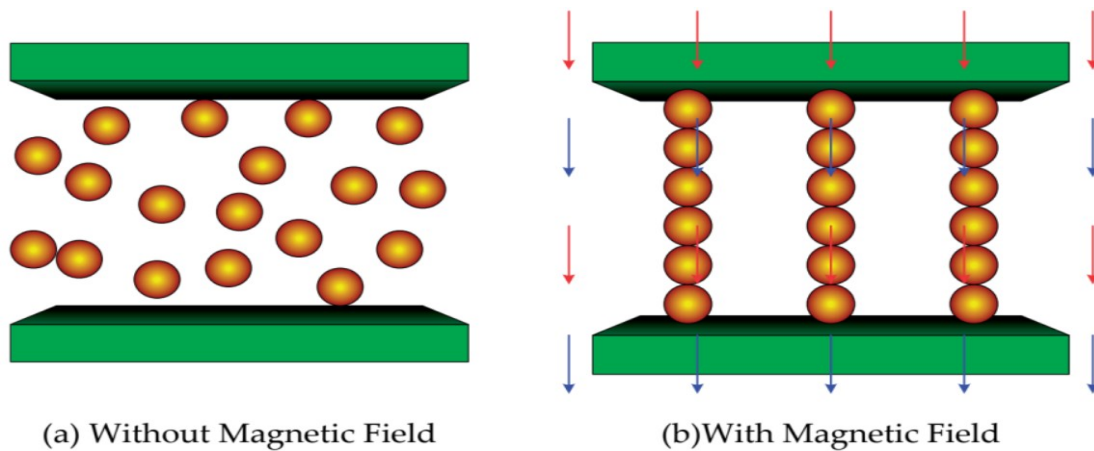
Figure 1.3 Magnetorheological materials' working principle [18]

The most prevalent MR materials are MR fluids (MRFs). The MRFs consist of three main components which are the base fluid, micron-sized ferromagnetic particles (typically Carbonyl iron powder to its high magnetic saturation) and additives. The fabrication process of MR fluids can be reduced into the mixing of all the fundamental constituents together. The ferromagnetic particles play a key role in the MR effect brought upon by the external magnetic field. The additives used in the fabrication of MR fluids, play an important role, and act as the stabilizer to prevent the sedimentation of particles in the carrier (base) fluid. Alongside the magnetic field strength, the rheological properties of MRFs highly depend on the size and concentration of the ferromagnetic particles and additives [18, 19]. The application of MR fluids is investigated in various fields including automotive industry as MR brakes and clutches [20, 21], building engineering as seismic resistors [22], and vibration control [23-25]. However, the MRF-based devices have sedimentation, sealing and environmental contamination problems [26] which degrade their wide spread application in industry.

To alleviate the shortcomings associated with MRFs, Magnetorheological elastomers (MREs), which are their solid analogues, are developed by incorporating the micro-sized ferromagnetic particles in a solid polymeric matrix. The first investigations into the MR effects of MR elastomers were conducted by Rigbi and Jilken [27]. While their MR effect might be slightly less than MRFs, the MREs prove high stability and do not have

sedimentation problems. The MREs consist of three fundamental constituents which include the ferromagnetic particles, synthetic rubber or elastomeric matrix and the additives. Because of high saturation limit of Carbonyl iron particles (CIPs) and hyper elastic behavior of silicon rubber, these materials are commonly used in fabrication of MREs as filler ferromagnetic particles and host matrix, respectively.

The fabrication of MRE samples generally consists of a three-stage process as shown in figure 1.4. First, the primary components, namely silicone rubber, silicone oil and carbonyl iron particles are thoroughly mixed. It should be noted that the ratios and proper amounts of each component relies on the desired density of the magnetic particles in the MRE sample. The prepared mixture is then degassed before being placed in a mold for the sample to be cured. The prepared MREs can then be divided into two different types based on two different fabrication curing methods [28]. If the mixture is cured in the presence of an external magnetic field, an anisotropic MRE sample is formed. In the anisotropic samples, chain-like structures are formed by the magnetic particles in the direction of the magnetic field in the final sample after the curing. If the mixture is cured in the absence of an external magnetic field, an isotropic MRE sample is formed. In the isotropic samples, the magnetic filler particles are distributed homogenously. Based on their structure, the anisotropic samples possess higher MR effects as compared to their isotropic analogues. However, the anisotropic samples present a challenging fabrication process involving a relatively strong magnetic field up to 1 T. Therefore, it is customary to fabricate and use the isotropic samples in most devices.

Numerous studies have been conducted on the dependence and variation of shear storage and loss moduli of MREs with respect to the varying magnetic field. The microstructure and viscoelastic properties alongside with the MR effect of different fabricated isotropic MRE samples were characterized and investigated by Gong et al. [29]. Various samples with different weight percentages of additives and carbonyl iron particles were fabricated and analyzed. According to Gong et al. [29], the isotropic sample with the 60 percent weight of CIPs and 20 percent weight of additives (silicone oil) possessed the best MR effect. The microstructure and viscoelastic properties of anisotropic MRE samples were characterized and analyzed by Chen et al. [30]. The

reported results indicate that the rheological properties and the microstructures of anisotropic samples highly depend on the applied magnetic field during the curing process. According to Chen et al. [30], the anisotropic MRE samples with higher curing magnetic field have higher MR effect.
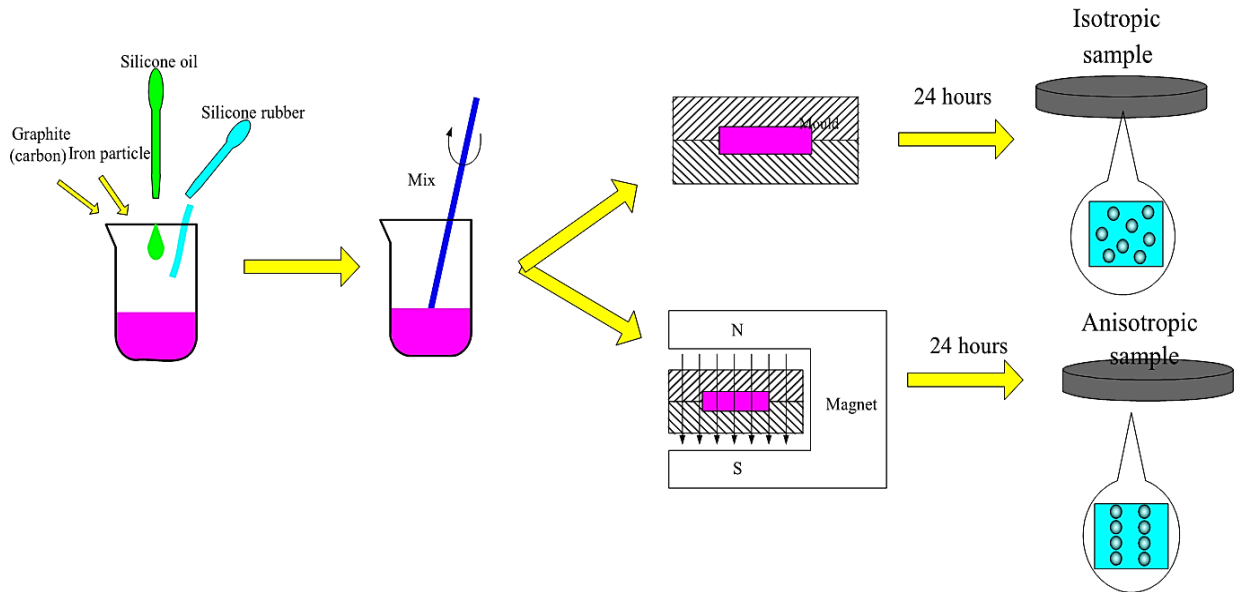
Figure 1.4 Fabrication process of MRE samples [31]

Among the other mechanical properties, the storage (stiffness) and loss moduli (damping) of MREs can be substantially and instantly varied under the application of an external magnetic field [32, 33]. Thus, spring and damping elements in conventional passive TVAs can be effectively replaced by MREs to develop MRE-based vibration absorbing systems for real-time vibration attenuation.

1.4 Magnetorheological Elastomer-based vibration absorbers

The MREs were benefitted in many devices and applications involving adaptive systems ranging from vibration isolators, variable impedance devices, force actuators and sensors [34]. One of the applications which gained a lot of research attention in the recent years is the development of adaptive tunable vibration absorbers. Different interesting MRE-based vibration absorber designs have already been investigated which utilize different working modes of the MRE samples including shear mode [13], squeeze mode [35], and

compression mode [36]. Figure 1.5 represents the various operation modes of MREs in the adaptive vibration absorbers, namely, the shear mode in (a), compression mode in (b) and squeeze mode as in (c).
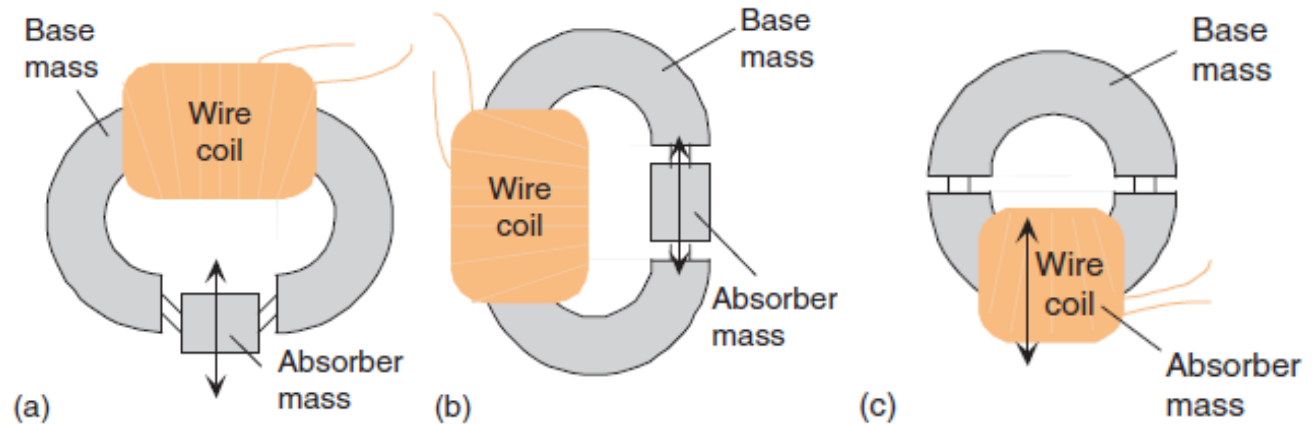
Figure 1.5 Working modes of MREs in adaptive vibration absorbers [36]

The first endeavors towards the adaptive tunable vibration absorbers involving the MREs were to design simple one-degree-of-freedom mass spring systems and incorporate the MREs as the variable stiffness spring. In this regard, a design for the adaptive vibration absorber using the MREs in shear mode was suggested, implemented and characterized by Ginder et al. [37]. The reported results indicate an adaptive frequency bandwidth of 500-610 Hz over the range of 0-560 mT magnetic field density. A similar design was later implemented and characterized by Deng et al. [13] which incorporated anisotropic MRE slabs with 70% mass ratio of CIPs. The vibration absorber reportedly attained a frequency shift from 55 Hz with zero electrical current in electromagnets to 81.25 Hz under the applied current of 1.5 Amp. The design was further improved and made compact by Deng and Gong [38], which worked in a frequency bandwidth of 27.5-40 Hz. A novel, simple and compact design was also proposed by Dong et al. [39], incorporating anisotropic MRE samples with 60% mass fraction of CIPs assembled inside a piston-cylinder system. According to Dong et al. [39], the implementation of a simple skyhook control law on the

experimental evaluation of the device revealed more than 25% vibration reduction in the host system. These early proposed designs are summarized and depicted in figure 1.6.

1. Cover, 2. guiderod, 3. Linear bearing
4. Magnetic conductor, 5. Shear plate, 6.
MREs, 7. Base, 8. Electromagnet
9. Mounting shell

(c)

(d)
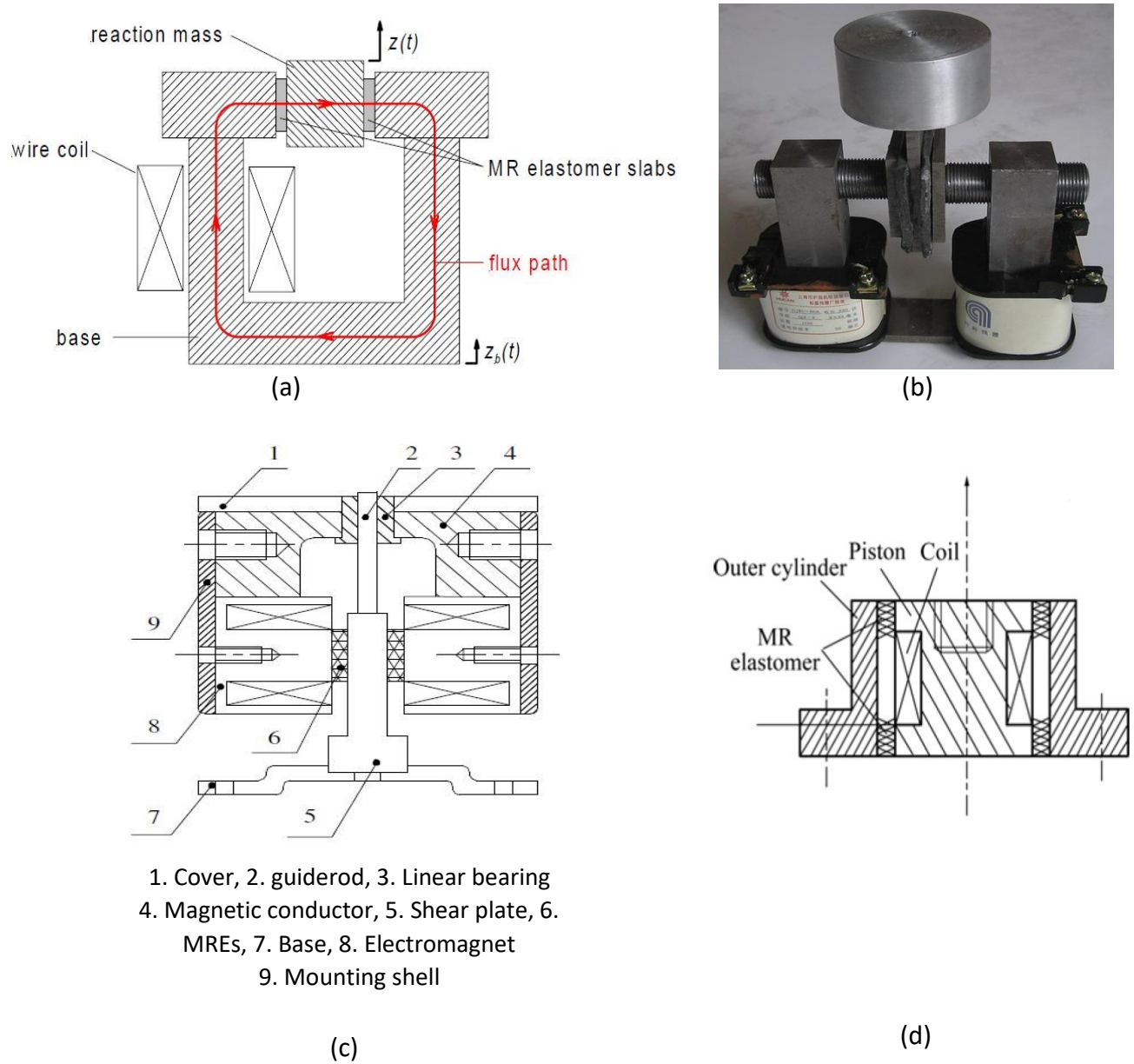
Figure 1.6 The first proposed designs for the MRE-based adaptive vibration absorbers; (a) Ginder et al. [37], (b) Deng et al. [13], (c) Deng and Gong [38], (d) Dong et al. [39]

A laminated adaptive vibration absorber incorporating MRE sheets was modeled, prototyped and characterized by Sun et al. [3]. It was reported that the device could be used for the adaptive vibration suppression in the low-frequency range of 3.2-19 Hz in the electric current range of -4 Amp to 4 Amp. Sun et al. [40], improved the proposed design by incorporating a self-sensing capability into the vibration absorber unit by introducing a self-inducing coil into the structure. Komatsuzaki et al. [41], also developed a self-sensing MRE-based adaptive vibration absorber by embedding a graphite-based elastomer in the MRE layers as a sensor. The results indicated that the self-sensing dynamic vibration absorber could operate in the frequency range of 25.8-37.4 Hz with the MRE samples of 40% volume density of CIPs. The developed self-sensing adaptive vibration absorbers by Sun et al. [40] and Komatsuzaki et al. [41] are depicted in figure 1.7.
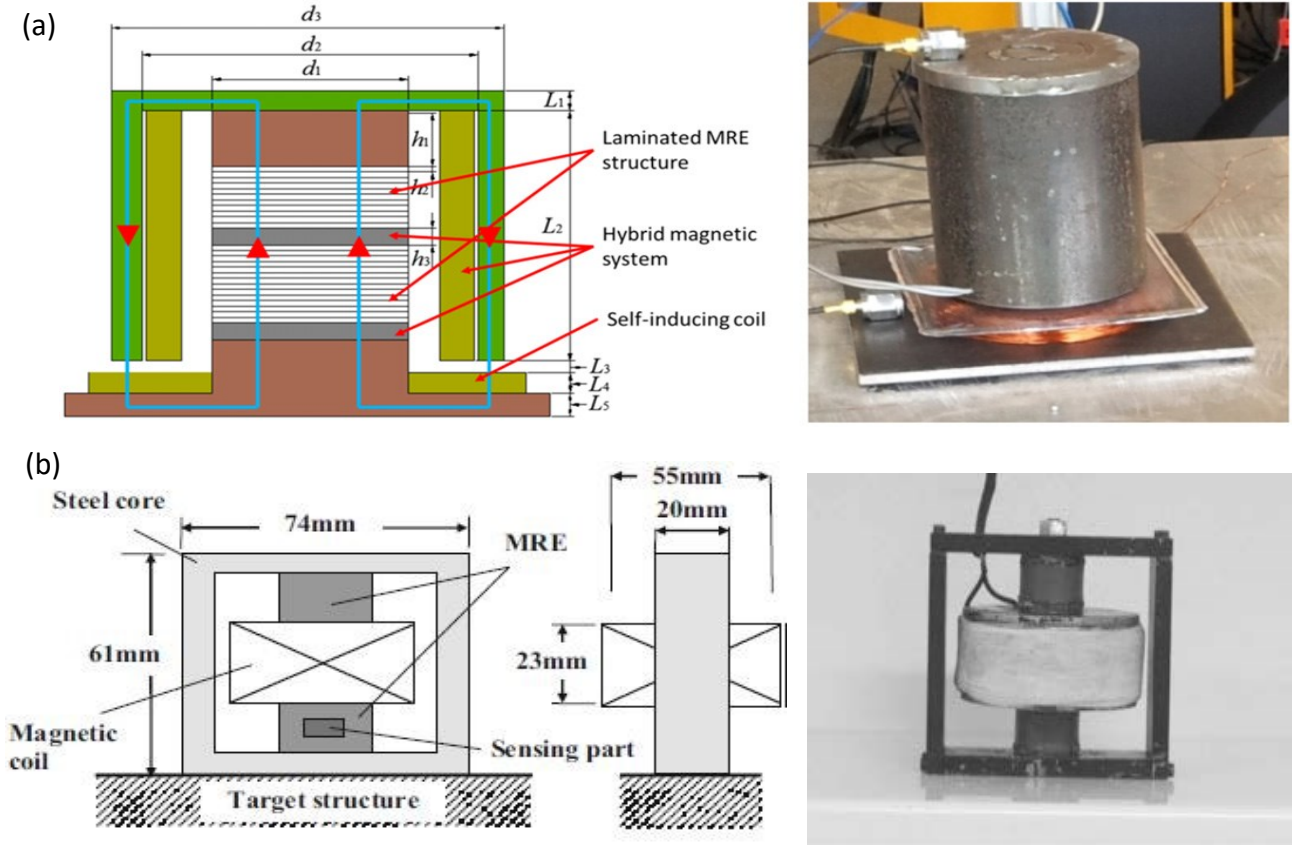
Figure 1.7 The self-sensing MRE-based adaptive vibration absorbers developed by: (a) Sun et al. [40] (b) Komatsuzaki et al. [41]

Various adaptive vibration absorbers were also developed and proposed which can be utilized in specific industrial applications. Xin et al. [15] combined a vibration isolation unit within an adaptive vibration absorbing unit to develop an adaptive vibration absorber for the powertrain mount systems (Figure 1.8). The experimental results indicated a natural frequency-shift of 22.7 Hz to 31.9 Hz in the electrical current range of 0-2 Amp. Liu et al. [42] developed an MRE-based semi-active dynamic vibration absorber for suppression of the longitudinal vibrations of the propulsion shaft systems in submarines (Figure 1.9). The reported experimental results indicate a natural frequency range of 43.09-56.88 Hz. Jang et al. [43] developed a practical compact adaptive vibration absorber which could be used in a plug-and-play fashion (Figure 1.10). The vibration absorber module proved to operate in the frequency range of 51.6-71.9 Hz under 0-340 mT magnetic field density. Yang et al. [44], developed a hybrid MRE-based adaptive vibration absorber, which can suppress the rotational and translational modes of unwanted excitations (Figure 1.11). The absorber which consisted of a stepper motor as the eccentric mass and a multilayer MRE pillar, can tune its rotational and translational natural frequency in the range of 2.99-4.45 Hz and 4.81-9.66 Hz, respectively, while the electrical current varies from -2 Amp to 2 Amp.
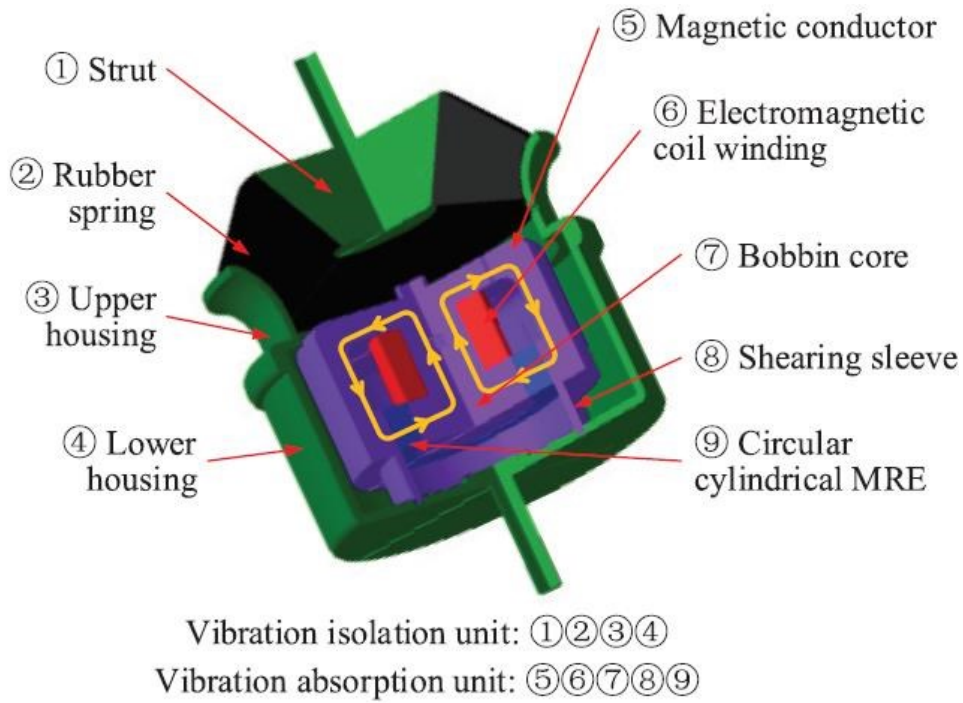
Figure 1.8 The adaptive vibration absorber developed by Xin et al. [15] for automotive powertrain mount systems
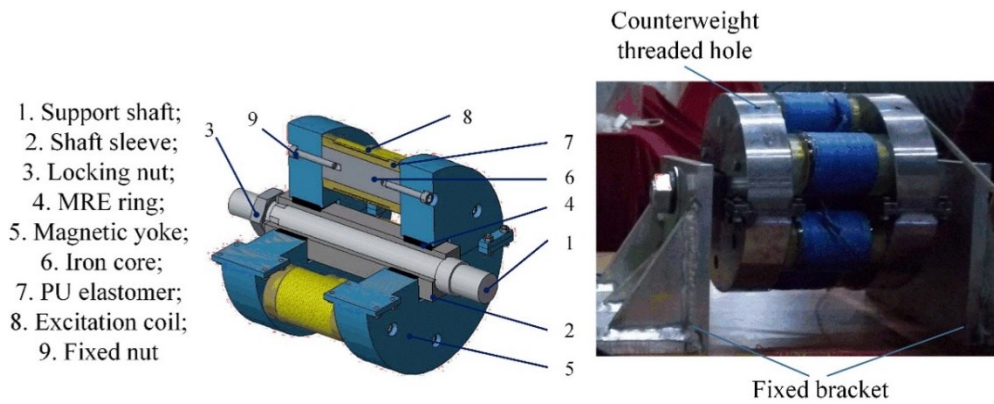
Figure 1.9 The adaptive MRE-based vibration absorber developed by Liu et al. [42] for suppression of longitudinal vibration of propulsion shaft systems
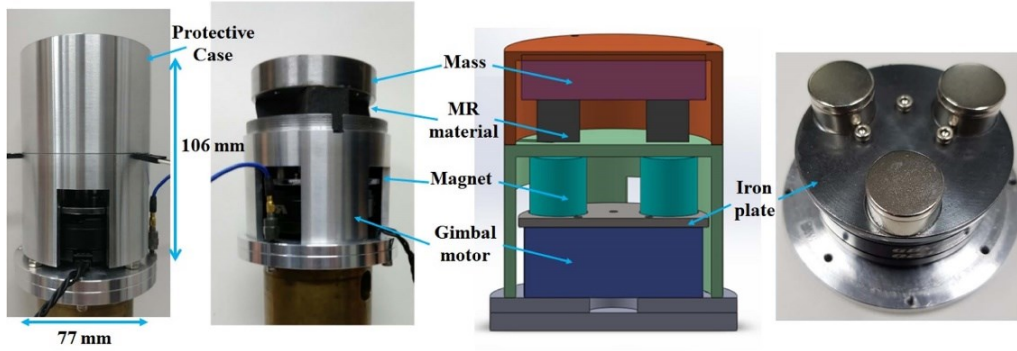
Figure 1.10 The compact, energy-efficient MRE-based adaptive vibration absorber developed by Jang et al. [43]
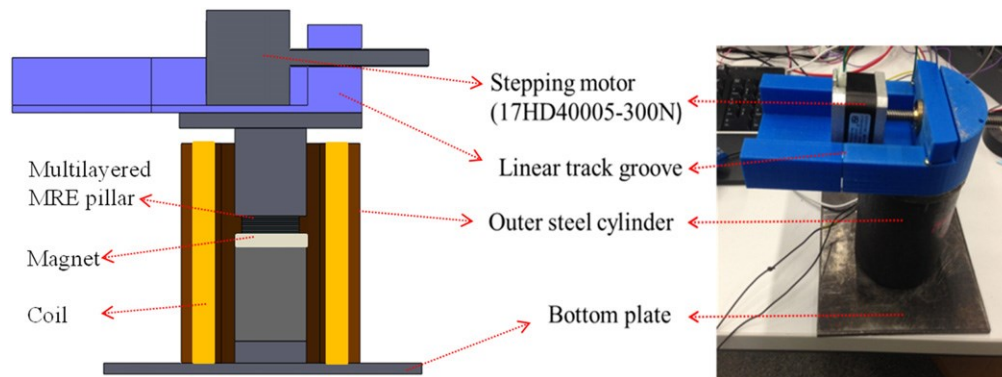
Figure 1.11 The hybrid MRE-based vibration absorber developed by Yang et al. [44]

While the dynamics of MRE-based sandwich structures have been extensively investigated, the adaptive vibration absorbers featuring MRE-based sandwich structures have not been studied yet. The MR materials in sandwich structures could be treated as viscoelastic materials with field dependent viscoelastic properties [45]. Research studies, on characterization and vibration modelling of passive sandwich beams comprised of elastic and viscoelastic layers, have been widely reported. The analytical model and solutions for the free vibrations of three-layered sandwich beams with viscoelastic core layer and thin elastic face layers have been examined [46, 47]. The forced transverse vibration of the three-layered sandwich beam with arbitrary boundary condition was also investigated [48], and an iterative numerical method for the free vibration solutions were subsequently considered for the case of fixed-fixed sandwich beam [49].

1.5 Current Study and Contributions

In the present work a novel design for SATVAs featuring MRE-based sandwich beam is investigated and an appropriate practical adaptive control-law is then established. To meet the mechanical and magnetic design constraints, the proposed design benefits from an additional steel layer in the middle of sandwich beam. This extra elastic layer will further reinforce the structure while increasing the magnetic field density in semi-active MRE layers. This novel design is well suited for suppression of lateral vibrations of continuous structures. In particular, the current design can be utilized to mitigate the vibrations induced on structural members which mostly occur in the low frequency range such as wind-induced vibrations in power transmission lines [50] . The finite element model of the proposed SATVA is first developed and then utilized to design the SATVAs with desired specifications. The designed SATVA is then fabricated and experimentally tested to evaluate its frequency response transmissibility and the shift in the natural frequency as well as to validate the developed FE model. With the verified FE model, a reduced-order equivalent mechanical structure of the vibration absorber is developed and subsequently an adaptive control-law is established to optimally control the vibration of an exemplary host structure.

1.6 Thesis Organization

This dissertation research is organized into five chapters, describing the outcomes and research findings in a systematic manner. The research studies and pertinent literature regarding the characterization, fabrication and different MRE-based adaptive vibration absorbers have been summarized in chapter 1.

Chapter 2 is dedicated to the detailed design of the proposed adaptive vibration absorber. First, the overall shape of the novel MRE-based semi-active adaptive vibration absorber structure is briefed. In the next step, the dynamic modeling of the structure is formulated based on developed Finite Element (FE) methods. The magnetic analysis of the structure is then described using the open source FEMM magnetic analysis software package. The design considerations of the structure and performance criteria are then established for the absorber apparatus and the final desired parameters are identified. Finally, a

parametric study was conducted to see the effect of different design parameters on the device performance and mechanical constraints.

The experimental study of the structure is provided in Chapter 3. First, the preparation of MRE samples in the laboratory is discussed. Then, the experimental tests conducted to evaluate the shear storage and loss moduli of MREs as well as its permeability are described. The experimental tests conducted on the fabricated electromagnets are also discussed. Finally, open-loop vibration tests on the overall assembly of the proposed semi-active adaptive tunable vibration absorber are detailed. Results of experiments are also used to verify the predicted performance of the absorber and developed FE models.

Chapter 4 includes the development of the adaptive control-law. A reduced-order equivalent model of the absorber is developed based on the open-loop results and characterized. The overall assembled host structure and SATVA system was then analyzed and the control objective is defined. Next, the background and assumptions on the Adaptive Kalman Filters (AKFs) are described. Finally, the adaptive phased-based control-law is established and the results are discussed.

The major findings and contributions together with some future remarks are discussed and summarized in Chapter 5.

Chapter 2: Design and Development of the MRE-based Semi-active Adaptive Tunable Vibration Absorber (SATVA)

2.1 Summary

The semi-active adaptive tuned vibration absorbers (SATVAs) can effectively attenuate the vibration over a wide range of frequencies compared with their passive counter parts. Despite the abundance of shape designs, SATVAs generally consist of a semi-active stiffness element and an oscillating mass.

In this chapter, a novel shape design is proposed, designed and developed for an adaptive semi-active vibration absorber based on MRE-based sandwich structures. In this design the MRE semi-active material is used as the semi-active stiffness elements in a sandwich structure on which two sets of electromagnets are mounted. First, the shape configuration for the sandwich structure of the SATVA is discussed. Then, the formulation of the dynamic Finite Element (FE) model to analysis the MRE-based sandwich structure is presented. Subsequently, the magneto-static magnetic FE model to study the magnetic field distribution generated by the electromagnets is presented. The final specifications, design constraints and identified design parameters with some remarks are then provided. A parametric study was also conducted to investigate the effect of different design parameters on design constraints and the performance of the SATVA.

2.2 SATVA featuring MRE-based Sandwich Structure

The proposed novel SATVA consists of a five-layered sandwich beam treated with two layers of isotropic MREs (25% particle volume fraction) as the viscoelastic layers sandwiched between three thin elastic steel plates as shown in figure 2.1. The steel plates are mainly under bending and longitudinal loading while the MRE-based core layers operate in shear mode and act as the variable stiffness elements. The sandwich beam is then integrated with two electromagnets bounded on the top and bottom elastic layers, forming a closed loop magnetic circuit with the beam including the middle MRE layer as the gap. In the proposed design each electromagnet comprises one U-shaped magnetic

core with two wire wound bobbins. The electromagnets are designed to provide the required magnetic field and also to serve as the oscillating active mass. The SATVA can be clamped at one end to the host structure while the electromagnets, can freely oscillate.

Attachment to host structure

- ▨ *Elastic thin steel plates*
- ▨ *MRE layer*
- ▨ *Electromagnets'steel Core*
- ⊠ *Electromagnet's coil*
- -- *Magnetic Flux*
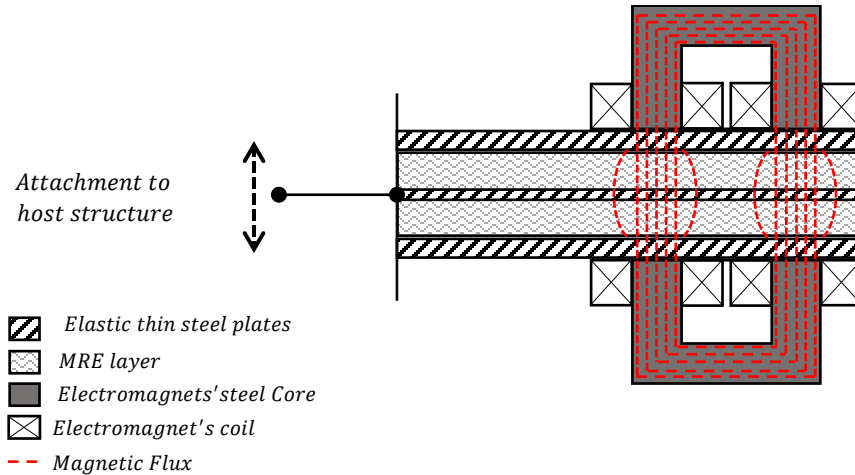
Figure 2.1 Schematic of SATVA

2.3 Model Development

The modelling of the proposed SATVA comprises two phases. In the first phase the electromagnets attached to the beam are treated as the oscillating mass of the absorber. The dynamic FE model of the proposed SATVA is then developed. The second phase addresses the magneto-static FE model of electromagnets to evaluate the generated magnetic flux density in the MRE upon application of the current to the electromagnet.

2.3.1 Formulation of the Dynamic FE Model

In this study, the dynamic finite element model of the proposed MRE-based SATVA has been developed considering some simplifying assumptions. The SATVA can be treated like a sandwich beam which is rigidly attached from one end to the host system which carries a point mass along with an equivalent moment of inertia representing the transverse displacements and rotation of the electromagnets. As depicted in Figure 2.2, the thicknesses of top, middle and bottom steel plates are denoted as h_1, h_3 and h_5, respectively, while the MRE layers' thicknesses are represented by h_2 and h_4.
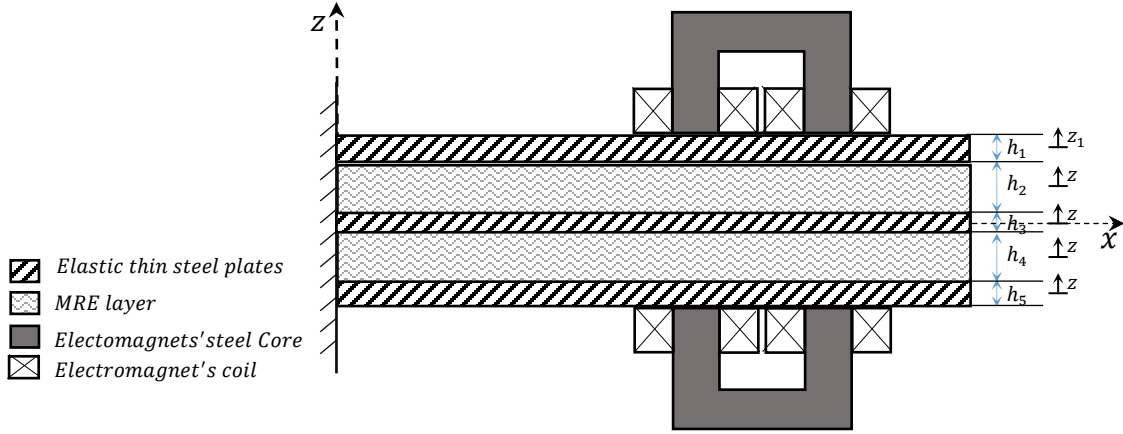
Figure 2.2 System parameters for SATVA

It is assumed that the thicknesses h_i of each layer are very small as compared with the length of the beam which allows the application of Classical Plate Theory. The thin elastic plates were modelled using Kirchhoff plate theory, which neglects the shear deformations. Taking into account the symmetry of the device, only longitudinal and transverse vibrations were considered. It is also assumed that the MRE layers undergo linear shear deformations throughout the thickness and that the normal stress is negligible in these viscoelastic layers. Furthermore, the transverse displacement is considered constant throughout the thickness of the structure and there is no slippage between layers.

According to Kirchhoff Plate Theory, the displacement field in the thin elastic plates can be expressed in the following form:

$$u^{(i)}(x,z,t) = u_i^0(x,t) - z_i \frac{\partial w(x,t)}{\partial x} \qquad ; \qquad i = 1,3,5$$

$$w(x,z,t) = w(x,t) \tag{2.1}$$

where u denotes the longitudinal displacement along the x axis, w represents the transverse displacement and u_i^0 denotes the longitudinal displacement of mid-layer of elastic thin plates. In the above formulation, superscripts $i = 1,3,5$ refer to the top, middle and bottom layers of the structure, respectively, and z_i is the local transverse coordinate system of each layer, origin of which lies at the mid-layer. Considering no slippage between adjacent layers in the sandwich structure, the following constraint should be applied.

$$u^{(i)}\Big|_{z_i = -h_i/2} = u^{(i+1)}\Big|_{z_{(i+1)} = +h_{(i+1)}/2} \qquad ; \qquad i = 1,2,3,4 \qquad\qquad (2.2)$$

It should be noted that the superscripts $i = 2,4$ refer to the viscoelastic MRE layers. Using zero slippage conditions as specified in Eq. (2.2) and considering linear shear strain throughout the viscoelastic layers, the transverse shear strain γ_{xz} and shear stress τ_{xz} in the MRE layers may be obtained with respect to the displacement fields in the elastic thin layers:

$$\gamma_{xz}^{(i)} = \frac{u^{(i-1)}\Big|_{z_i = -h_i/2} - u^{(i+1)}\Big|_{z_i = +h_i/2}}{h_i} + \frac{\partial w}{\partial x} = \frac{d_i}{h_i}\frac{\partial w}{\partial x} + \frac{u_{(i-1)}^0 - u_{(i+1)}^0}{h_i}$$

$$\tau_{xz}^{(i)} = G^{(i)}\gamma_{xz}^{(i)} \qquad\qquad\qquad\qquad ; \ i = 2,4$$

$$(2.3)$$

where $d_i = h_{(i-1)}/2 + h_i + h_{(i+1)}/2$, and $G^{(i)}$ represents the complex shear modulus of MRE layers.

Assuming that the MRE core layers work in linear viscoelastic region (which is justified for small beam deformation), the complex shear modulus of viscoelastic layers can be written as follows:

$$G^{(i)} = \ G'_{(i)} + jG''_{(i)} \qquad\qquad\qquad ; \ i = 2,4 \qquad\qquad\qquad (2.4)$$

where $G'_{(i)}$ and $G''_{(i)}$ represent the storage and loss moduli of the MRE material, both of which vary with respect to the change in the external magnetic field.

2.3.1.1 Development of the 5-layer MRE-based Sandwich Beam Element

To formulate the finite element model, a one-dimensional, 5-layer MRE-based sandwich beam element having two nodes and five degrees of freedom (DOFs) per node has been developed as shown in Figure 2.3 for an arbitrary element e of the beam. The DOFs include transverse displacement, w, and longitudinal displacements at mid planes of the thin elastic layers (u_1^0, u_3^0, u_5^0) along with the slope, $\theta = dw/dx = w_{,x}$.
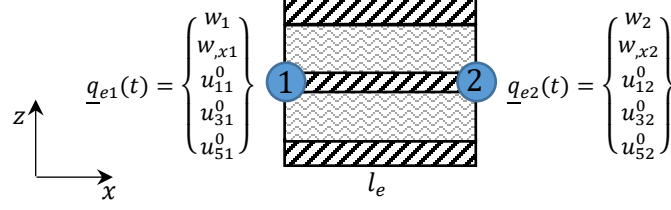
Figure 2.3 One-dimensional sandwich beam element

The transverse and longitudinal displacement fields within the elements can be expressed in terms of the nodal degrees of freedom vector at each node $j = 1,2$, $\underline{q}_{ej}(t) = \{w_j, w_{,xj}, u^0_{1j}, u^0_{3j}, u^0_{5j}\}^T$ and shape function vectors as follows:

$$u^0_i(x,t) = \underline{N}_{ui}(x)\underline{q}_e(t)$$

$$w(x,t) = \underline{N}_w(x)\underline{q}_e(t) \qquad ,i = 1,3,5$$

$$\underline{q}_e(t) = \begin{Bmatrix} \underline{q}_{e1} \\ \underline{q}_{e2} \end{Bmatrix} \qquad\qquad\qquad (2.5)$$

where the vector $\underline{q}_e(t)$ represents the elemental degrees of freedom (10-DOF element) for the arbitrary element e depicted in Figure 2.3. The shape function vectors are functions of variable x and can be described as:

$$\underline{N}_{u1}(x) = [0,0,(1-\bar{x}_e),0,0,0,0,\bar{x}_e,0,0]$$

$$\underline{N}_{u3}(x) = [0,0,0,(1-\bar{x}_e),0,0,0,0,\bar{x}_e,0]$$

$$\underline{N}_{u5}(x) = [0,0,0,0,(1-\bar{x}_e),0,0,0,0,\bar{x}_e]$$

$$\underline{N}_w(x) = [(1-3\bar{x}_e^2+2\bar{x}_e^3), l_e(\bar{x}_e-2\bar{x}_e^2+\bar{x}_e^3),0,0,0,(3\bar{x}_e^2-2\bar{x}_e^3), l_e(-\bar{x}_e^2+\bar{x}_e^3),0,0,0]$$

$$\bar{x}_e = \frac{x}{l_e} \qquad\qquad\qquad (2.6)$$

in which $\bar{x}_e$ represents the non-dimensional variable, normalized with respect to the element's length l_e. Therefore, for the span of $x \in [0, l_e]$, we have $\bar{x}_e \in [0,1]$.

The total energy of the element per unit width is the sum of the energies of its five sublayers. The total potential and kinetic energy per unit width of the elements, namely V and T, can then be described as:

$$T = T_1 + T_2 + T_3 + T_4 + T_5$$

$$V = V_1 + V_2 + V_3 + V_4 + V_5 \tag{2.7}$$

where V_1, V_3 and V_5 represent axial strain energies (per unit width) of the top, middle and bottom thin elastic plates, respectively, while V_2 and V_4 denote the shear strain energies (per unit width) of core layers. Also, T_1, T_3 and T_5 are kinetic energies (per unit width) associated with the transverse and axial motions of the top, middle and bottom plates, respectively, while T_2 and T_4 are computed by considering rotational and transverse motions of the core layers. The energy functions for the element of length l_e can now be formulated as:

$$V_i = \frac{l_e}{2} \int_0^1 \int_{-h_i/2}^{+h_i/2} \sigma_{\bar{x}_e}^{(i)} \varepsilon_{\bar{x}_e}^{(i)} d\bar{x}_e dz \ , \qquad i = 1,3,5$$

$$V_j = \frac{l_e}{2} \int_0^1 \int_{-h_j/2}^{+h_j/2} \tau_{\bar{x}_e z}^{(j)} \gamma_{\bar{x}_e z}^{(j)} d\bar{x}_e dz \ , \qquad j = 2,4$$

$$T_i = \frac{l_e}{2} \int_0^1 \int_{-h_i/2}^{+h_i/2} \rho_i \left(\left(\dot{u}^{(i)} \right)^2 + (\dot{w})^2 \right) d\bar{x}_e dz \ , \qquad i = 1,3,5$$

$$T_j = \frac{l_e}{2} \int_0^1 \rho_j \left(h_j (\dot{w})^2 + I_j \left(\dot{\gamma}_{\bar{x}_e z}^{(j)} \right)^2 \right) d\bar{x}_e \ , \qquad j = 2,4 \tag{2.8}$$

where ρ_i and ρ_j represent the volumetric mass densities of the elastic and core layers, respectively. Also, in the above formulation $I_j = h_j^3/12$ represents the second moment of area (per unit width) for the MRE core layers, which are computed with respect to local mid-layer longitudinal axes.

Now, the governing dynamic equations of motion for the MRE-based sandwich beam element can be derived by combining Eq. (2.7) and (2.6) and utilizing Lagrange formulation as:

$$\frac{d}{dt} \left(\frac{\partial L}{\partial \dot{q}_e^k} \right) - \frac{\partial L}{\partial q_e^k} = Q_k, \qquad k = 1, \dots, 10 \tag{2.9}$$

where Lagrangian $L = T - V$ and q_e^k denotes the k-th component in the elemental degrees of freedom vector $\underline{q}_e(t)$. The governing equations of motion of the proposed sandwich element may be subsequently formulated into the FE form as:

$$\underline{\underline{M}}_e \ddot{\underline{q}}_e + \underline{\underline{k}}_e \underline{q}_e = \underline{f}_e \tag{2.10}$$

where $\underline{\underline{M}}_e$, $\underline{\underline{k}}_e$ and $\underline{f}_e$ denote element mass matrix, element stiffness matrix and element nodal force vector, respectively. Finally, the elemental mass and stiffness matrix alongside with the element force vector are assembled to derive the system governing equations in FE form as:

$$[M]\{\ddot{\delta}\} + [K^*]\{\delta\} = \{f\}$$

$$\{\delta\} = \bigcup_{e=1}^{N_e} \underline{q}_e \tag{2.11}$$

in which $\{\delta\}$ is the system DOF vector which is obtained from assemblage of the N_e elemental DOF vectors. The mode shapes and natural frequencies of the system can be subsequently evaluated as the eigenvectors and eigenvalues of Eq. (2.11) in the absence of the external force. It is noteworthy that the meshing of sandwich structures with the sandwich element lengths l_e of order of millimeters yields accurate results. In the present work, the length of elements was chosen as 1 millimeter.

2.3.2   Formulation of the Magneto-Static FE Model

The viscoelastic properties of MREs strongly depend on the subjected external magnetic field. Therefore, a set of electromagnets must be designed to provide a sufficient magnetic field in the MRE layers of the vibration absorber. To this end, the magnetic FE model of electromagnets was developed and designed using the open source FEMM software package [51]. Magneto-static analyses were then conducted on the electromagnets in a 2D planar environment. figure 2.4 shows the FEMM software environment in which the electromagnets were modeled with the sandwich beam forming the gap. The governing equations for the magneto-statics are as follows:

$$\nabla \times \mathbf{H} = \mathbf{J}$$

$$\mathbf{B} = \mu \mathbf{H}$$

$$\mathbf{B} = \nabla \times \mathbf{A} \tag{2.12}$$

where $\mathbf{B}$, $\mathbf{H}$, $\mathbf{J}$, μ, and $\mathbf{A}$ denote the magnetic flux density, magnetic field intensity, current density, magnetic permeability, and magnetic vector potential of the medium under

investigation, respectively. Considering Eq. (2.12), the final constitutive equation can be formulated as:

$$\nabla \times \left(\frac{\nabla \times \mathbf{A}}{\mu} \right) = \mathbf{J}$$

(2.13)

which has been utilized in the Finite Element tool embedded in the FEMM to analyze the electromagnets. In a 2D environment, the magnetic vector potential, $\mathbf{A}$, reduces to the component A_z normal to the plane. Therefore, the first-order triangle finite element with the magnetic potentials as the DOFs are utilized as depicted in Figure 2.5.
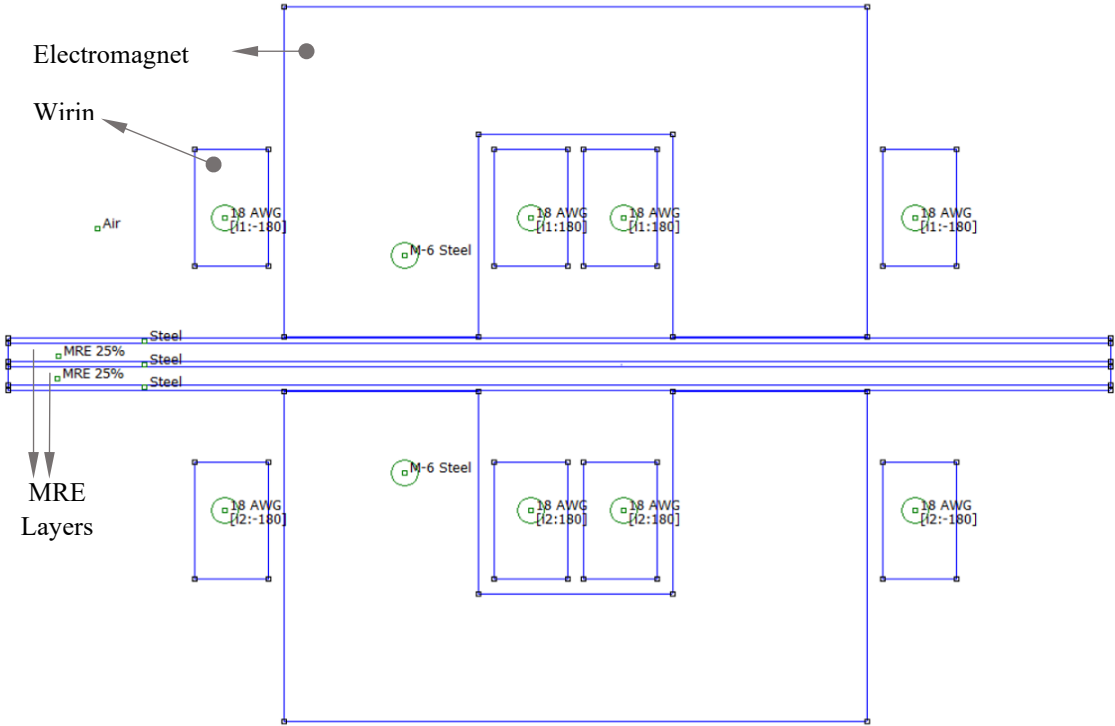
Figure 2.4 Electromagnets' modeling in FEMM
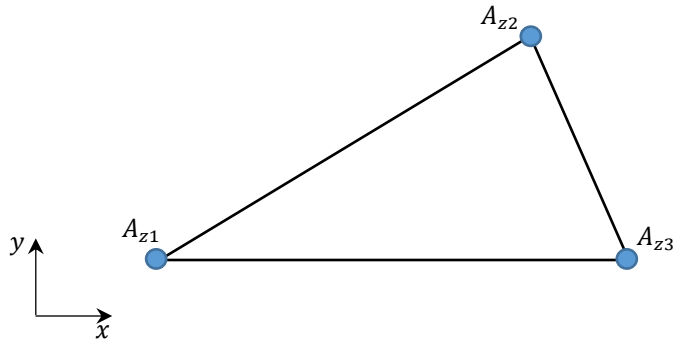
Figure 2.5 The magnetic triangular finite element

The medium in the model is first considered to be air and triangular meshing with 22485 nodes was generated in an unbound domain approximated by an open boundary with the radius of 25 cm around the electromagnets. The distribution of magnetic flux density for $I = 5\ \mathrm{Amp}$ with 6 mm air gap is shown in Figure 2.6.
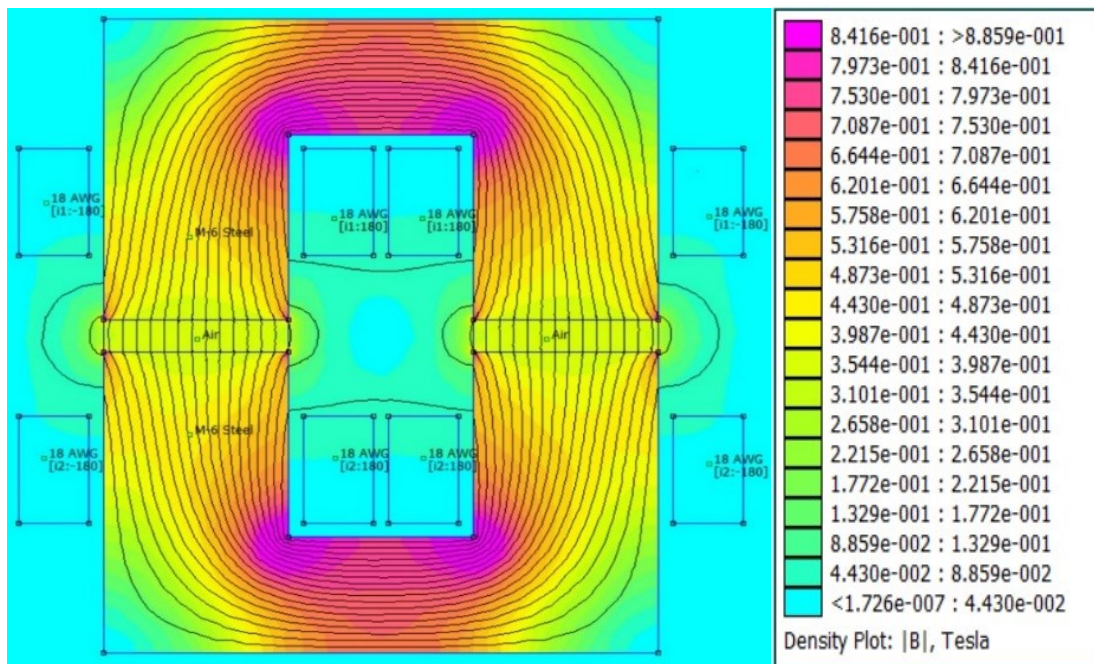
Figure 2.6 Distribution of Magnetic flux density with a 6 mm air gap ($I = 5\ Amp$)

2.4 Design Considerations and Final Specifications

The following design criteria has been considered for the proposed MRE-based SATVA:

- The maximum static tip deflection of the absorber caused by the electromagnets should be within the geometrical linearity region.

- The maximum stress resulted in the steel layers must be within the material linearity region.

- Taking into account that the coils warm up depend on the operating time and applied electric current, the maximum allowable electric current is set at 6 Amp.

The design goal is to maximize the operating frequency range of the SATVA. For this purpose, various configurations were investigated for the MRE sandwich beam and the electromagnet. It is noteworthy that compared with the conventional three-layered sandwich beam with MRE core layer, the function of the middle thin steel layer which was added considered in the proposed configuration is twofold. In addition to reinforcing the beam to withhold the electromagnets' mass, the middle steel layer also increases the permeability in the gap which results in the increase of magnetic flux in the MRE layers. In order to design the absorber apparatus, the FE model of the electromagnet alongside with the FE model for the MRE sandwich beam were utilized. Various trial and error procedures have been conducted to obtain the feasible parameters for both the MRE sandwich beam and the electromagnets. It should be noted that the length of the beam, layers' thickness, elastic layers' materials, dimensions and position of the electromagnets, number of wiring turns in each of the coils and size of the wire were the design parameters considered in the present study. The dimensions and parameters addressing the final design of the absorber apparatus considered in the present work are provided in Table 2.1 and Figure 2.7. The performance of the designed MRE-based SATVA is also provided in Table 2.2.
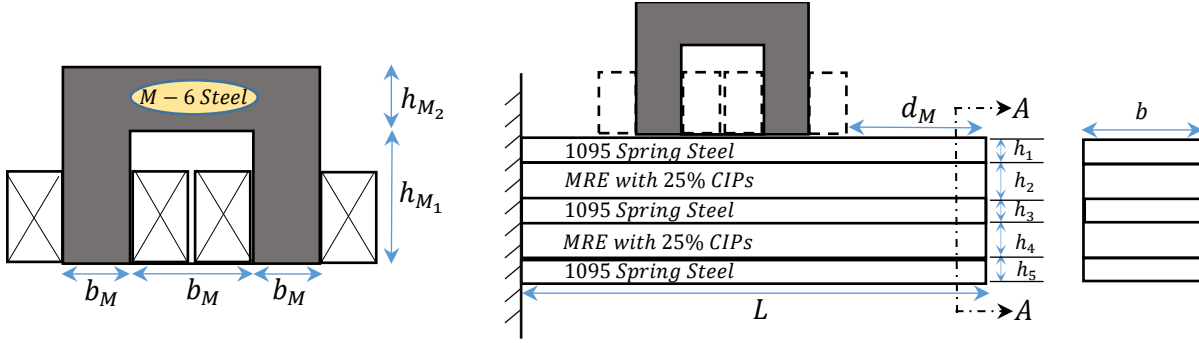
Figure 2.7 SATVA dimensions and parameters

Table 2.1 System parameters and their finalized values

Sandwich Structure			Electromagnets		
Symbol	*Description*	*Value*	*Symbol*	*Description*	*Value*
h_1, h_3, h_5	Thickness of steel layers	1 mm	N	Number of coil windings per bobbin	180 Turns
h_2, h_4	Thickness of MRE layers	3 mm	—	Coil windings' wire	18 AWG
b	Width of Sandwich Structure	20 mm	b_M	Design Dimension (Figure 2.7)	3.175 cm
d_M	Position of electromagnets	65 mm	h_{M_1}	Design Dimension (Figure 2.7)	3.45 cm
L	Length of beam	180 mm	h_{M_2}	Design Dimension (Figure 2.7)	2.175 cm
—	Loss factor of steel layers	0.2873	—	Electromagnets' Mass	2.153 kg
—	Fabricated Sandwich beam's mass	0.387 kg	—	Electromagnets' Moment of inertia	3.47 g.m^2

Table 2.2 SATVA performance obtained using the developed FE model

Performance Parameters	Value
Tip deflection of beam shape structure	14.2 mm
Maximum Axial Stress in Steel layers	134 MPa
Magnetic field range upon MRE layers	0-600 mT
Field off-state natural frequency of SATVA	6.19 Hz
Frequency range of vibration absorber	9.68 %

As it can be realized the tip displacement is less than 10% of the beam length and also the maximum stress in steel layers is well below the yield strength 1095 spring steel. The maximum magnetic field of up to 600 mT can be generated which results in almost 10% variation in absorber frequency.

2.5 Parametric Study

The developed FE models (will be validated using experimental study in the next chapter) can be effectively utilized to investigate the effect of different design parameters on the SATVA performance. In this study, the variations in the maximum axial stress in the elastic layers and the frequency range of the absorber were studied by varying different design parameters including elastic layers thickness and the position of the electromagnets on the beam structure. To generate sufficient magnetic flux density in the MRE layers, the overall thickness of the sandwich structure was considered to be 9 mm. First, the effect of the variations of thickness of the elastic layers on the frequency range and the maximum axial stress were investigated. For the given location of the electromagnets as provided in Table 2.1 (position from free end, $d_M = 65 \text{ mm}$), the effect of thickness of elastic layers (top and bottom elastic layers are assumed to have equal thickness) on the maximum stress and frequency range are investigated and results are shown in Figure 2.8.

As it can be realized, the maximum stress and frequency range of the absorber decreases as the thickness of the elastic layers increase. Thus, for the optimal design with high frequency ranges and low axial stresses in layers, the solution must lie in the direction of

steepest descent in the maximum stress surface profile. As predictable by Eq (2.1), results show that the steepest descent direction for the maximum stress is the line for which the thicknesses of elastic layers are equal.
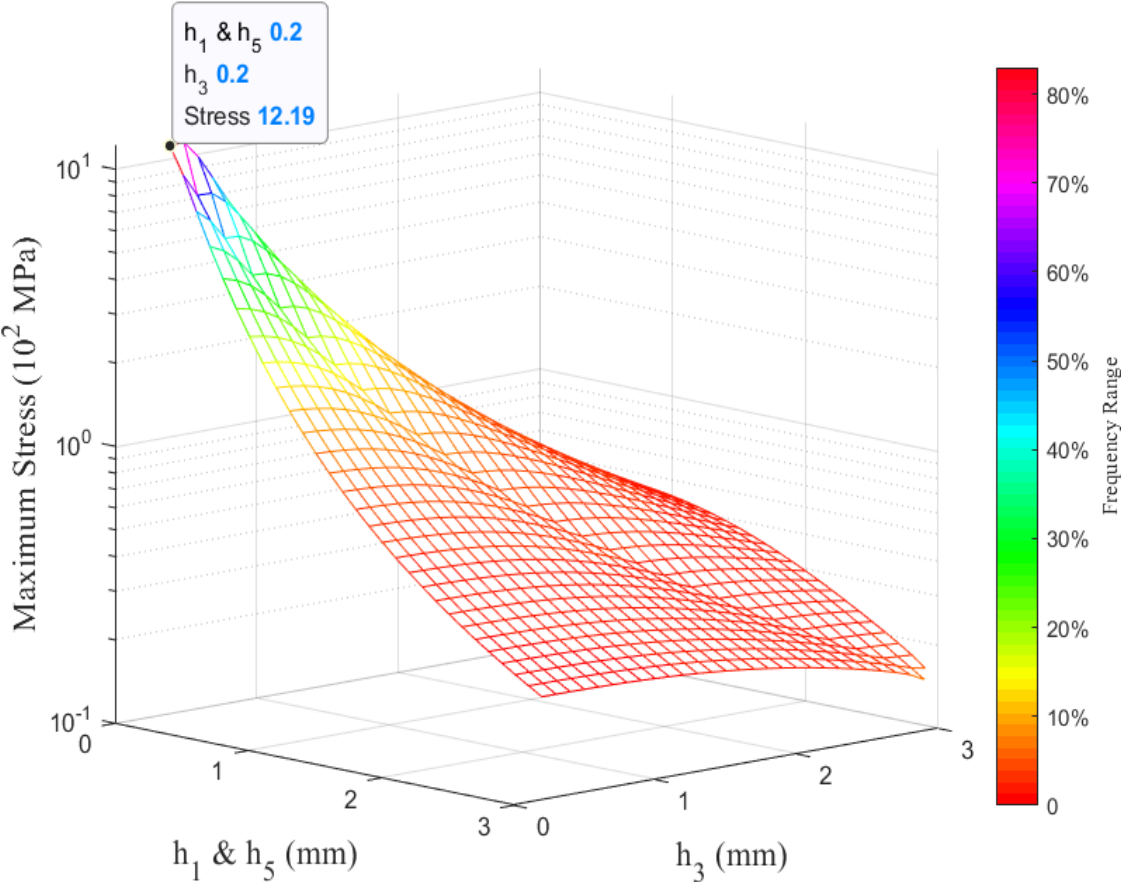
Figure 2.8 Effect of thickness of elastic layers on maximum stress and frequency range

Now considering equal thicknesses for the elastic steel layers, the effect of the position of the electromagnets and thickness of elastic steel layers on the SATVA performance was studied and results are shown in Figure 2.9. It is noted that the electromagnet position is measured from the tip of the beam as shown in Figure 2.7.
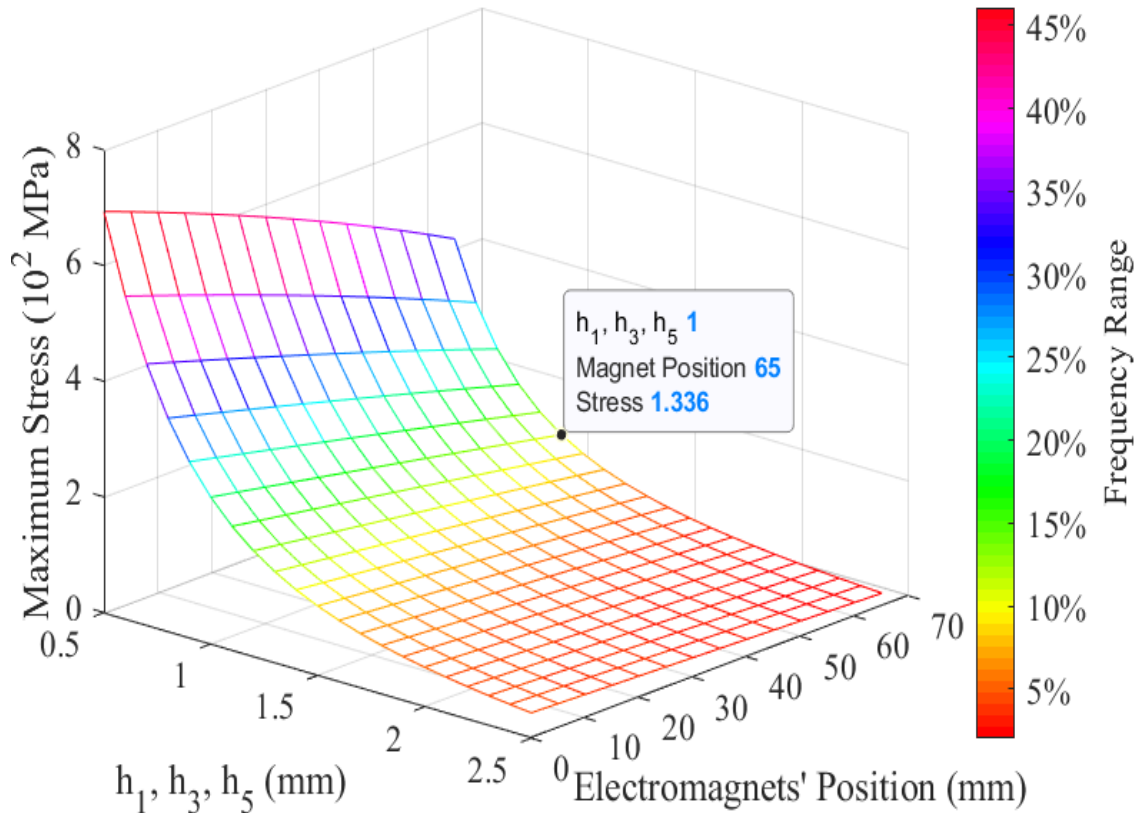
Figure 2.9 3D view of effect of thickness of elastic layers and magnets' position on the maximum stress and frequency range

Results suggest that by moving electromagnets toward the tip of the absorber, the frequency range can be increased up to nearly 30%, however this will cause excessive stress in elastic layers beyond their yield strength which may cause permanent bending of the beam. The yield strength of elastic layers is around 400 MPa. Considering a safety factor of around 3, the maximum allowable stress in elastic layers would be nearly 140 MPa. Considering Figure 2.9, this would render the thickness of elastic layers and position of electromagnet as 1 mm and 65 mm (from tip) as shown by solid circle in the figure which is indeed the design parameters selected for the proposed MRE-based SATVA. For better clarification, the 2D representation of variation in maximum stress and frequency range of the proposed adaptive absorber with respect to the thickness of elastic layers and position of electromagnet are also demonstrated in Figure 2.10.
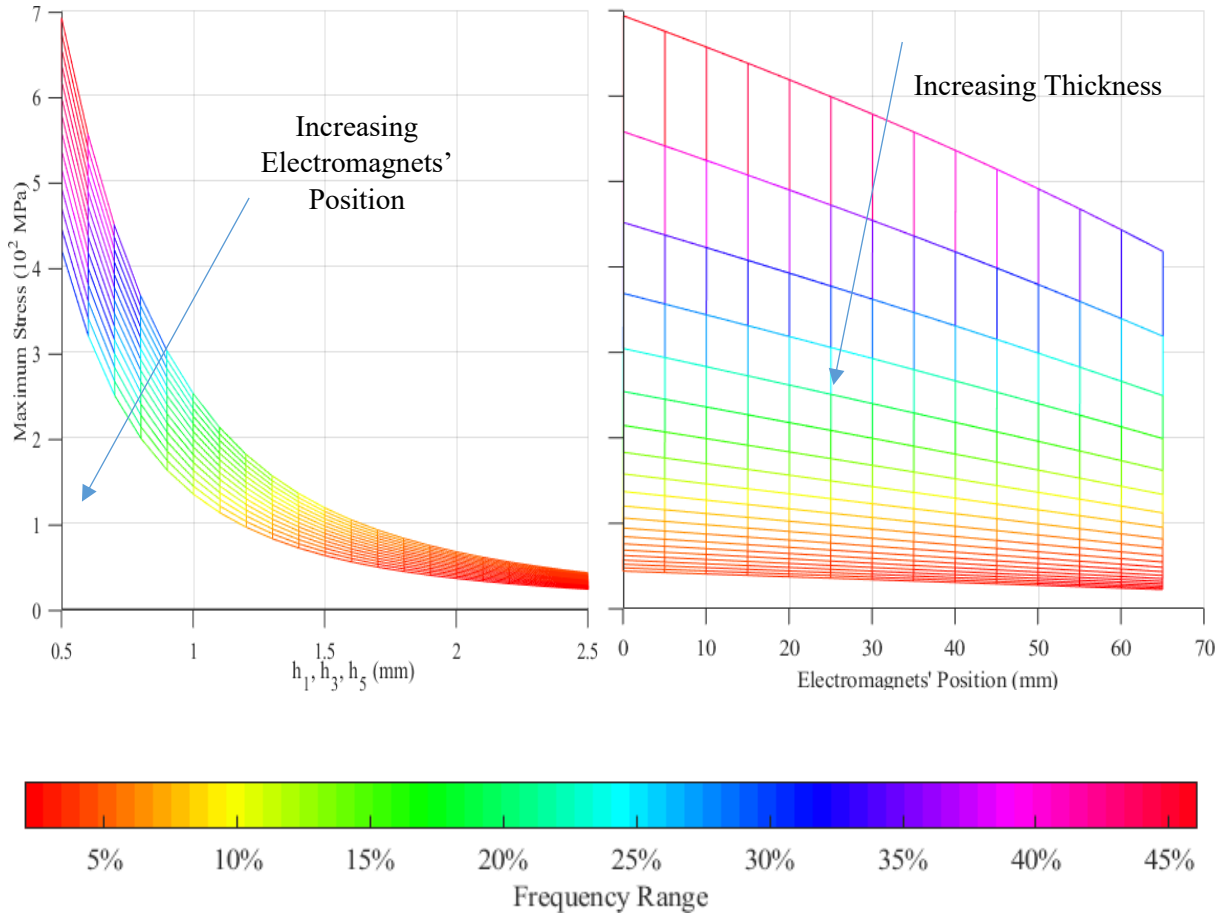
Figure 2.10 2D view of effect of thickness of elastic layers and magnets' position on the maximum stress and frequency range

2.6 Conclusion

In this chapter, a novel MRE-based adaptive vibration absorber has been developed and designed. To this end, a five-layered MRE-based sandwich structure was proposed with two U-shaped electromagnets mounted on it. The FE models for the mechanical and magnetic analysis of the proposed STAVA are developed to check and verify the magnetic and mechanical constraints of the structure. The final design confirms nearly 10% frequency range of the absorber while satisfying the maximum stress and displacement constraints. A final parametric study was finally conducted to investigate the effect of different design parameters on the maximum stress induced and the frequency range.

Chapter 3: Experimental Study

3.1 Summary

To evaluate the frequency shift-property of the proposed SATVA and also to validate the developed FE models, the SATVA system is fabricated and open-loop magnetic and vibration tests are conducted. In the following, first the fabrication and experimental characterization of MRE samples are described. This is followed by the fabrication of electromagnets and the validation of the magnetic FE model along with the experimental evaluation of relative magnetic permeability of MRE samples. Finally, a vibration test has been conducted to characterize the fabricated MRE-based SATVA system and to validate the developed FE models.

3.2 Fabrication and Characterization of MRE Samples

The two core layers in the proposed SATVA are made of isotropic MRE with 25% volume fraction of magnetic particles. The MREs are fabricated using mixture of silicon rubber and carbonyl Iron Particles (CIPs) as the host matrix and fillers, respectively. The low viscosity Eco-flex™ 00-20 silicon rubber was chosen as it provides better distribution, easy mixing and degassing of MRE samples. As Fillers, spherical CIPs provided by BASF SQ® with average of 3.9-5 μm in diameter were used.

The fabrication can be divided into three major steps; mixing, degassing and curing. First, based on the 25% volume fraction of CIPs in the final sample, required amounts of silicon rubber and CIPs were mixed for about 3 minutes to form a homogeneous final solution. The solution was placed and degassed in the vacuum chamber under 28 inHg for about 5 minutes. Finally, the mixture was poured into rectangular mold and left for 24 hours to be cured in room temperature before being used as the MRE layers in SATVA.

To model the viscoelastic properties of the MRE layers under varied applied magnetic field, oscillatory shear tests were conducted on the fabricated isotropic MRE samples. The tests were performed using an advanced rotary parallel plate rheometer (Discovery HR-3, TA instrument) equipped with embedded magneto-rheology accessory as depicted

in Figure 3.1. As the absorber operates at low frequency range the effect of frequency on storage modulus has been ignored.
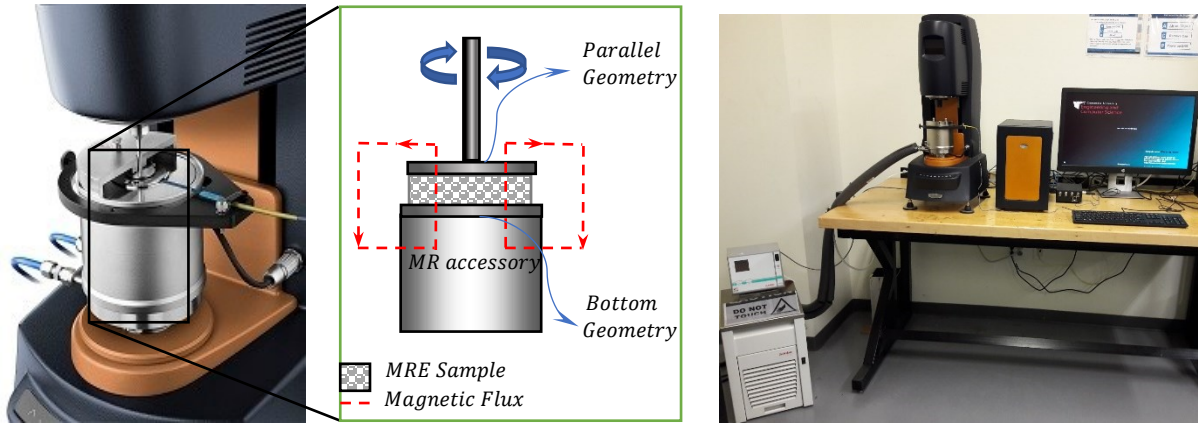
Figure 3.1 Characterization test bed (Discovery hybrid rheometer)

The variation of storage modulus and loss factor of MRE material with respect to the applied flux density is shown in Figure 3.2 for the driving frequency of 0.2 Hz and the strain amplitude of 0.1%. Based on Figure 3.2, while the storage modulus changes considerably upon the application of the magnetic field, the change in loss factor can be neglected. It is noted that MRE samples generally demonstrated linear viscoelastic behavior for strain amplitudes under 0.15%. A polynomial function of order 4 was subsequently used to accurately curve fit the actual experimental storage modulus data as:

$$G'(B) = p_1 B^4 + p_2 B^3 + p_3 B^2 + p_4 B + p_5 \quad [\text{kPa}] \tag{3.1}$$

in which constant coefficients p_1, p_2, p_3, p_4, p_5 are found to be -1283, 1904, -271.2, 73.84, 55.19, respectively, by minimizing the error between the simulation data from Eq. (3.1) and experimental data using the Least square minimization technique. It should be noted that coefficient of determination under the fitted polynomial becomes 99.99% while for the quadratic and cubic polynomial curves it becomes 98.67% and 99.73%, respectively. Both the experimental data and the fitted relation are shown in Figure 3.2. It is noted that the material model in Eq. (3.1) and point by point loss factor for the MRE sample were

utilized in Eq. (2.4) for the semi-active beam elements in the magnetic gap to account for the variation of the stiffness of the structure under the magnetic flux density.
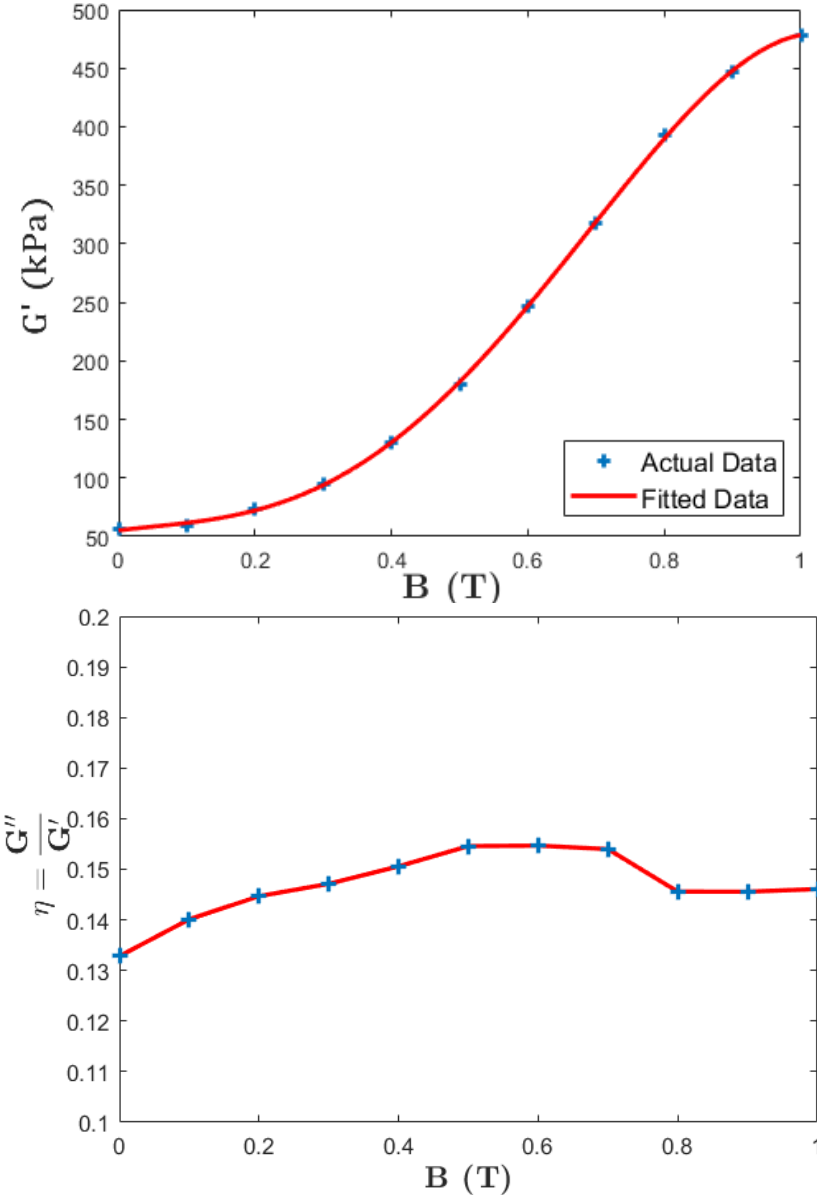
Figure 3.2 Storage modulus and loss factor variation with magnetic flux density for isotropic MRE with 25% volume fraction of CIPs

3.3 Fabrication and Magnetic Study of Electromagnets

To generate the required magnetic field in the MRE layers, with the sandwich structure forming the gap, a set of U-shaped electromagnets were designed and fabricated. In order to minimize the loss of the generated magnetic field due to eddy currents, the steel cores for the electromagnets were made by attaching thin laminates of thickness of 3 mm each, using 3M Epoxy Adhesive. For the wiring, bobbins of rectangular cross section were 3D printed using Onyx material. The bobbins were then wound with 18 AWG wires.

To verify the electromagnets' performance, their generated magnetic flux density was measured using gaussmeter and compared with the developed magnetic FE model in a 6 mm air gap as shown in Figure 2.6. The results for the magnetic flux densities in the middle of the air gap under $I = 2.5 \text{ Amp}$ and $I = 5 \text{ Amp}$ are provided in Table 3.1.

Table 3.1 Magnetic flux densities in center of a 6 mm air gap

	Exp.(mT)	FEM (mT)
$I = 2.5 \text{ Amp}$	180.0	181.4
$I = 5.0 \text{ Amp}$	367.0	363.2

As it can be realized, the predicted results for the magnetic flux densities using FE model are in good agreement with the experimental data. Then, using a 6 mm pierced MRE sample as the gap, the magnetic flux density was measured in the sample by the gaussmeter placed through the sample. Comparing the magnetic flux measurements for the air gap and the MRE sample, the relative permeability for the MRE samples with 25% volume fraction CIPs was experimentally measured as $\mu_r \approx 1.412$. The relative permeability of MRE samples was then utilized in the magnetic modelling of SATVA. Based on the relative magnetic permeability of MRE layers, the magnetic flux densities at the center of MRE layers under left and right side of U-shaped electromagnets were evaluated using magnetic static FE model developed in FEMM. The results for $I = 2, 4, 6 \text{ Amp}$ are provided in Table 3.2 which are consequently used in the FE model to

establish a relation between the increase of electrical current and the increase in the magnetic field. Also, the distribution of magnetic flux density for $I = 6\text{ Amp}$ is shown in Figure 3.3. As it can be realized, under applied current 6 Amp, the magnetic flux density of 600 mT can be generated at the center of the MRE layers in the proposed SATVA. It is also noted that the two MRE layers are symmetrically located with respect to the center of the sandwich beam as shown in Figure 2.7, thus the induced magnetic flux density is the same for both layers.

Table 3.2 Magnetic flux densities in center of semi-active MRE layers

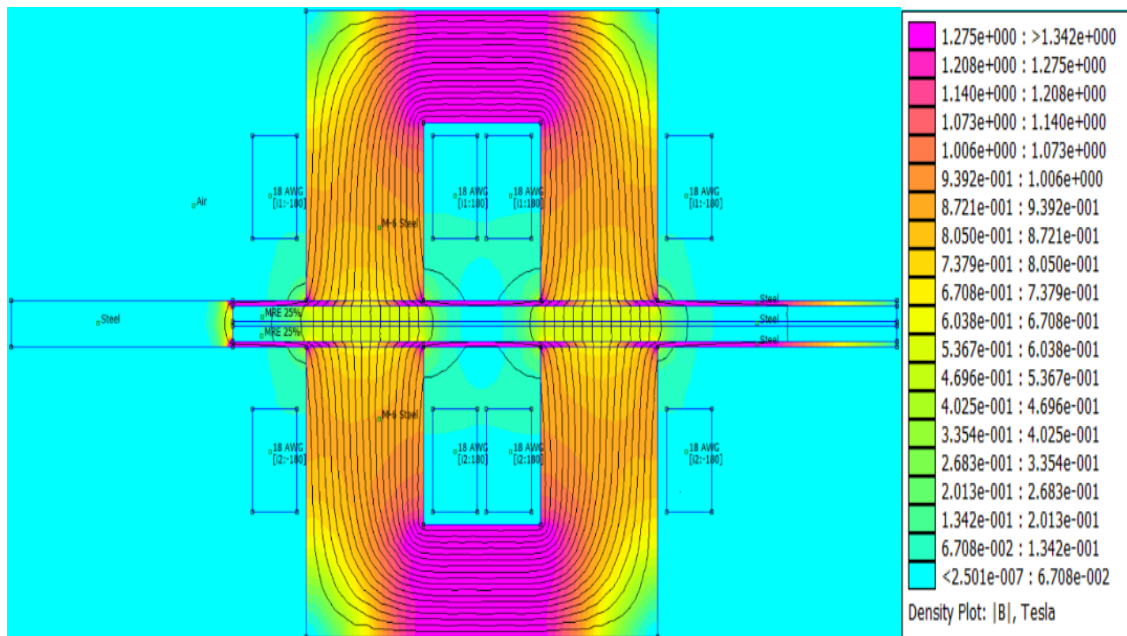|	Left side(mT)	Right side(mT)
$I = 2.0\text{ Amp}$	195.7	197.6
$I = 4.0\text{ Amp}$	397.7	399.8
$I = 6.0\text{ Amp}$	597.3	600.0

Figure 3.3 Distribution of Magnetic flux density in SATVA ($I = 6\ Amp$)

35

3.4 Vibration Test Bed Configuration

To verify the proposed MRE based SATVA's frequency-shift property, the 5-layer beam-like sandwich beam was fabricated and then integrated with the electromagnets. The absorber was then mounted as a cantilever beam on the shaker to measure the natural frequency of the fabricated SATVA. Two accelerometers, one at the support and the other one at the tip of the sandwich beam are installed. The single-axis accelerometer at the support measures the input acceleration to the system, while the miniature accelerometer (weighing 2 grams) installed on the tip of the beam was used to measure the tip acceleration of the absorber as the output of the system. The frequency response function (FRF) was then evaluated as the ratio of the output to the input acceleration. A DC power supply was also utilized to apply desired currents to electromagnet to evaluate the variation of the absorber's natural frequency under different applied currents. The fabricated MRE-based SAVA and the test-rig are shown in Figure 3.4.

3.5 Vibration Test Results

The vibration absorber was excited at the base with sinusoidal harmonic vibration under a constant acceleration amplitude of $0.1 \, \mathrm{m.\,s^{-2}}$ swept in the range of 2 to 20 Hz frequency using the vibration controller and shaker setup shown in Figure 3.4(b). The Frequency Response Function (FRF) was then derived from the measurements. In particular the FRF for the acceleration transmissibility of the vibration absorber (ratio of output to input acceleration) was analyzed to evaluate the natural frequency of MRE-based SATVA. The transmissibility FRFs were obtained under different currents applied to the electromagnets to investigate the shift in the natural frequency of absorber. Using the DC power supply shown in Figure 3.4(b) the input currents to the electromagnets' wiring were set to $I = 2, 4, 6 \, \mathrm{Amp}$ and the performance of the SATVA was investigated. Table 3.3 provides the natural frequencies and loss factors measured under different applied currents and their comparison with those predicted using the developed FE model. Figure 3.5 also shows the comparison of experimental transmissibility and that predicted by the FE model under applied current 0 and 6 Amp. It is noted that using half power bandwidth the loss factor was approximately found to be 0.29 and 0.25 from the experimental transmissibility in the absence of the magnetic field and presence of the maximum

magnetic field, respectively. According to the theoretical model the change in the loss factor due to the magnetic field is negligible. However, the change in the experimental loss factors, may be attributed to the decrease of damping of the silicon rubber with the increase of the working temperature due to heat generation in the electromagnets which is not considered in the theoretical model.
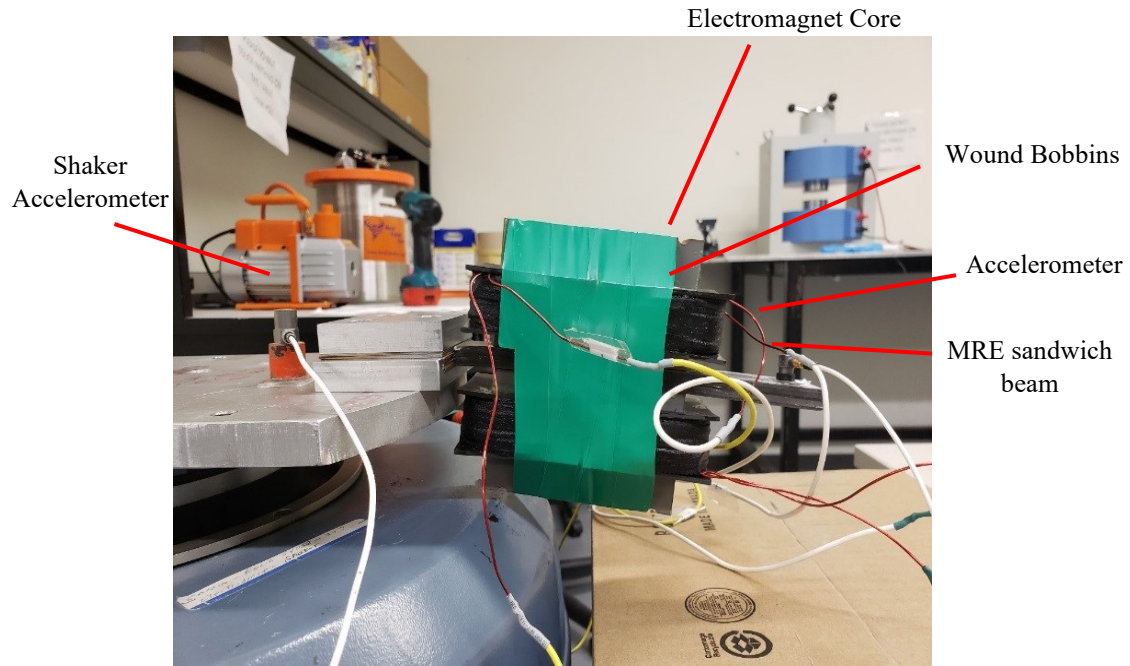
(a)
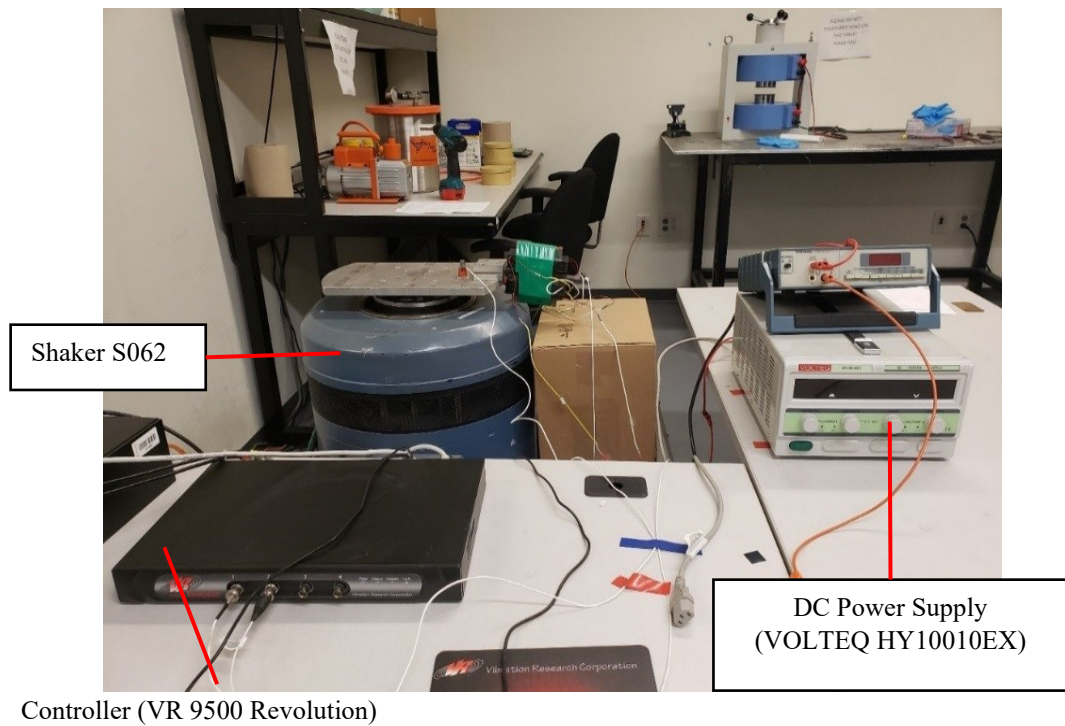
(b)

Figure 3.4 (a) Proposed SATVA (b) Vibration test Setup

Results provided in Table 3.3 and Figure 3.5 show that the developed FE models for the sandwich beam and electromagnets can accurately predict the natural frequency of the MRE-based SATVA as well as the transmissibility of the absorber under varying applied current. The developed model can thus provide guidance on the development of different types of SATVA incorporating MRE sandwich at the early stage of the design. While the proposed MRE-based SATVA can provide nearly 10% shift in the natural frequency at low frequency ranges, the developed model can be effectively utilized to design MRE sandwich beam type SATVA to operate at higher frequency ranges. It is noted that the experimental natural frequencies are slightly greater than those obtained using the developed FE model. This is likely due to the small portion of magnetic flux density which pass through steel layers along the length of the beam and eventually cross through the MRE layers at other part of the beam, resulting in further increase of beam stiffness. In simulation, this leakage of magnetic flux density has been ignored and MRE sections directly under the electromagnet have been activated. Moreover, the effect of adhesive used to bind the MRE layers to the elastic layers in sandwich beam has been ignored in FE modeling. The very thin layers formed by adhesive may also have contributed to the overall stiffness of the structure and thus slight increase in the natural frequency.

Table 3.3 Natural Frequency and Loss Factor of SATVA; Exp vs. FE model

	Natural Frequency (Hz)			Loss Factor		
	Exp.	FEM	Error (%)	Exp.	FEM	Error (%)
$I = 0.0$ Amp	6.46	6.19	4.36	0.2867	0.2509	12.49
$I = 2.0$ Amp	6.57	6.30	4.11	0.2784	0.2556	8.190
$I = 4.0$ Amp	6.84	6.47	5.41	0.2597	0.2580	0.6546
$I = 6.0$ Amp	7.03	6.79	3.41	0.2543	0.2598	2.163
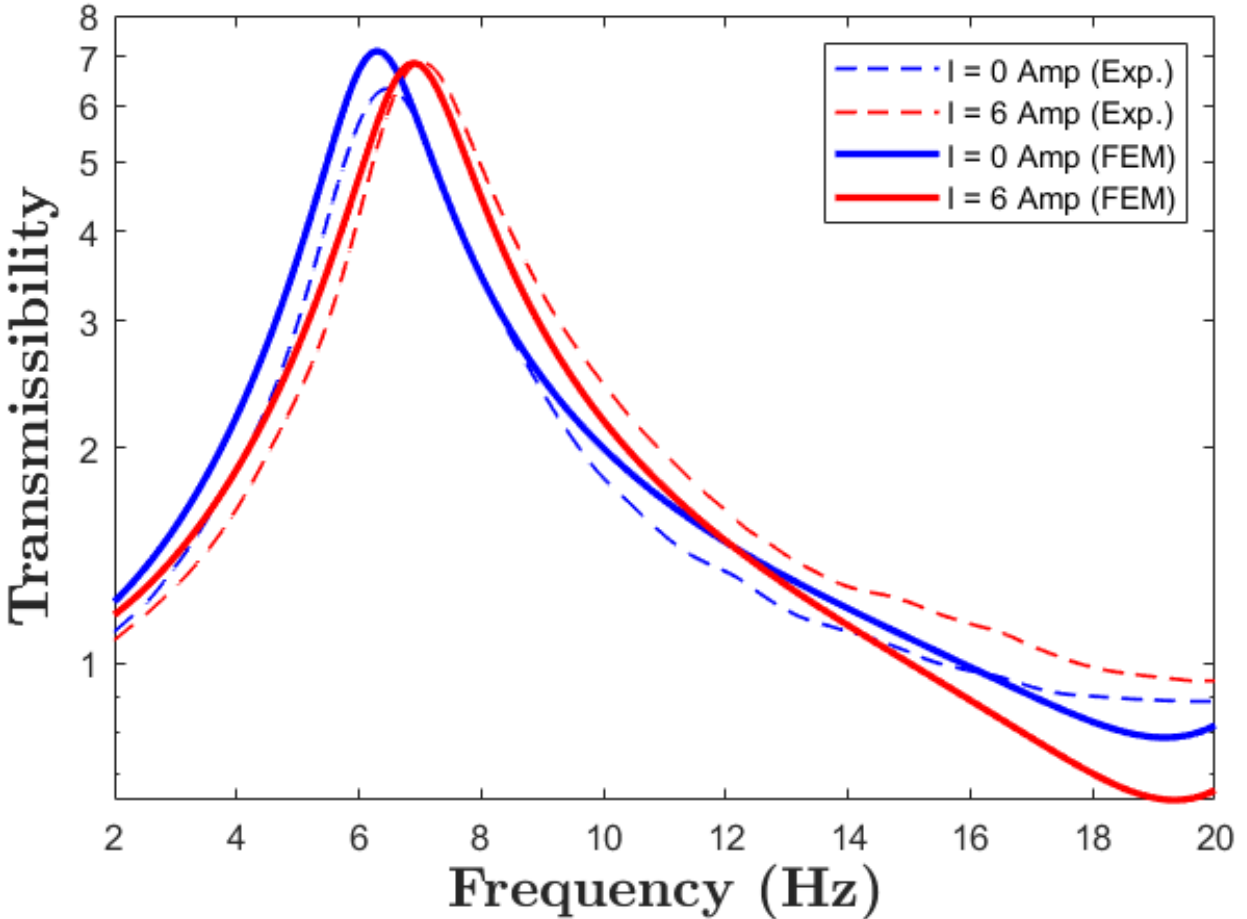
Figure 3.5 Frequency response open-loop study of the system (Experiment vs. FE model)

3.6 Conclusion

The novel MRE-based adaptive vibration absorber previously developed was fabricated and assembled. Different experiments were designed to characterize the MREs, the magnetic circuit and the proposed SATVA. The developed FE models for the mechanical and magnetic study of the vibration absorbers were then verified using experimental results. Vibration test conducted on the fabricated SATVA apparatus provides nearly 9% shift in its natural frequency by increasing the current from 0 to 6 Amp which agrees with that predicted by the FE model.

Chapter 4: Development of a phase-based control strategy based on Adaptive Kalman Filtering (AKF)

4.1 Summary

The goal of implementing the semi-active adaptive vibration absorbers are to effectively attenuate the unwanted vibrations of the host structures under wide range of excitation frequencies. To this end, it is of utmost importance for an effective, simple and practical control law to be developed for the industrial applications. There are noises and disturbances associated in with the sensors and system responses in the real-time applications. Also, the sensors implementation and maintenance costs associated with the system increase as the number of sensors increase for the feedback. Therefore, the conventional controllers may not possess optimal performance for the industrial and real-life applications.

In this chapter, an adaptive phase-based control strategy has been developed to suppress the vibration of a host structure under varying tonal excitation. The proposed SATVA has been modeled as an equivalent lumped system based on the experimental open-loop study in the previous chapter. The host structure (representing a continuous structure) has also been modeled as an equivalent single DOF system based on the fundamental mode of the structure. With the overall 2-DOF assembled system, a control strategy has been then developed based on the simplified dynamics of the equivalent system. An adaptive recursive noise estimator has been integrated in the developed control law. Finally, the frequency-tracking ability of the adaptive vibration absorber is investigated to demonstrate the performance of the proposed control strategy.

4.2 Development of the equivalent lumped mass model of the SATVA

In this section an equivalent lumped model of the proposed semi-active vibration absorber is derived. First, the point impedances for the two lumped and continuous models are analyzed based on the finite element formulation of the SATVA. Then the equivalent lumped model is both magnetically and mechanically characterized based on the experimental results of the fabricated vibration absorber. Finally, the point impedance

response of the experiment-based lumped model and the developed FE dynamic model of SATVA were compared and investigated to verify the equivalency of the models.

4.2.1 Analytical Model

As mentioned before, the proposed SATVA comprised of five layers in which two MRE core layers are sandwiched between three thin elastic reinforcing steel sheets. To develop the equivalent lumped model for the SATVA, the dominant fundamental natural frequency of the structure is used. The schematic of the pre-designed SATVA and the equivalent lumped model are shown in figure 4.1.
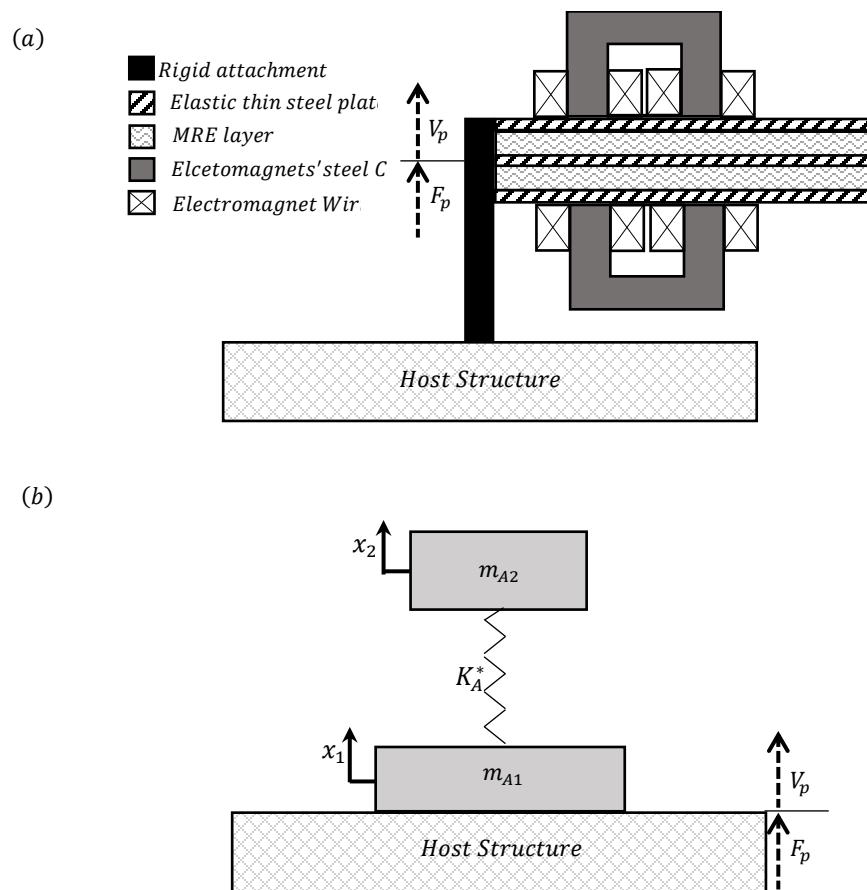
Figure 4.1 a) SATVA b) Equivalent 2DOF model

As discussed in Section 2.3, the governing equations of motion of the system in finite element form can be formulated as:

$$[M]\{\ddot{\delta}\} + [K^*]\{\delta\} = \{f\} \tag{4.1}$$

Where $[M]$ and $[K^*]$ denote the mass and complex stiffness matrices while $\{\delta\}$ and $\{f\}$ represent the global DOFs of the structure and the corresponding nodal forces.

Considering both lumped and continuous SATVA systems as equal, the point impedances at the base of the two systems are to be compared. To this end, the lumped and continuous systems are subject to base harmonic forces of magnitude F_p and radial frequency ω.

Applying the clamped-free boundary conditions with the base transverse excitation as depicted in figure 4.1, the point impedance of the continuous SATVA can be formulated from the governing equations of motion. With N_n denoting the number of nodes in FE model, the reduced-order form of equation (4.1) is used by neglecting the rotational and longitudinal DOFs of the node at the clamped end of the SATVA. The impedance of SATVA can be formulated as:

$$\{f\} = \{F_p, 0, \dots, 0\}^T e^{i\omega t}; \ \dim(\{f\}) = 5N_n - 4$$

$$\{\delta\} = \left[[K^*] - \omega^2 [M]\right]^{-1}\{f\}$$

$$\frac{F_p}{V_p} = \frac{f(1)}{(i\omega)\delta(1)} \tag{4.2}$$

The point impedance of the equivalent lumped model of the vibration absorber at the attachment to the host structure can be formulated using the following equations of motion:

$$\begin{cases} m_{A1}\ddot{x}_1 + K_A^*(x_1 - x_2) = F_p e^{i\omega t} \\ m_{A2}\ddot{x}_2 + K_A^*(x_2 - x_1) = 0 \end{cases}; \ K_A^* = K_A(1 + i\eta_A) \tag{4.3}$$

Where m_{A1}, m_{A2} represent the equivalent lumped masses while K_A^*, K_A and η_A represent the equivalent complex stiffness, storage modulus and loss factor of the simplified model as shown in figure 4.1(b). Considering the harmonic motion for the system, the point impedance of the equivalent lumped model can be calculated as follows:

$$\frac{F_p}{V_p} = \frac{F_p}{(i\omega X_1)} = i\omega \frac{\left(\frac{m_{A1} + m_{A2}}{m_{A1}}\right)(1 + i\eta_A)\omega_A^2 - \omega^2}{\frac{1}{m_{A1}}\left((1 + i\eta_A)\omega_A^2 - \omega^2\right)}; \quad \omega_A = \sqrt{\frac{K_A}{m_{A2}}} \tag{4.4}$$

4.2.2 Characterization of the equivalent model

The point impedance of the equivalent lumped model should be in good agreement with that of the original continuous model over the working frequency range by matching the mass $(m_{A1} + m_{A2})$, first natural frequency (ω_A in eqn (4.4)) and its associated average loss factor, η_A, for the equivalent lumped system to those of the fabricated system. It should be noted that the mass of the clamped section of the fabricated beam is not considered in the overall mass of the structure.

The polynomial functions can be used to curve fit the experimental data for the natural frequencies provided in Table 3.3 using least square minimization technique to find the relationship between the electrical current (input to the system) and the fundamental natural frequency (output of the system) as:

$$f_A(I) = (-4.85 \times 10^{-3})I^3 + (4.875 \times 10^{-2})I^2 + (-2.21 \times 10^{-2})I + 6.46 \quad [\text{Hz}] \tag{4.5}$$

Based on the experimental values from the fabricated device, the equivalent parameters have been identified to have equivalent point impedance and provided in Table 4.1. The absolute value of the point impedance of the equivalent model is also compared with the beam-like absorber in field-off state as shown in figure 4.2.

Table 4.1 Equivalent system parameters

I(Amp)	m_{A1}(kg)	m_{A2}(kg)	K_A ($\times 10^3$N/m)	I(Amp)	m_{A1}(kg)	m_{A2}(kg)	K_A ($\times 10^3$N/m)
0	0.8939	1.4032	2.3125	4.0	0.8494	1.4477	2.6755
2.0	0.8773	1.4198	2.4216	6.0	0.7957	1.5014	2.9334
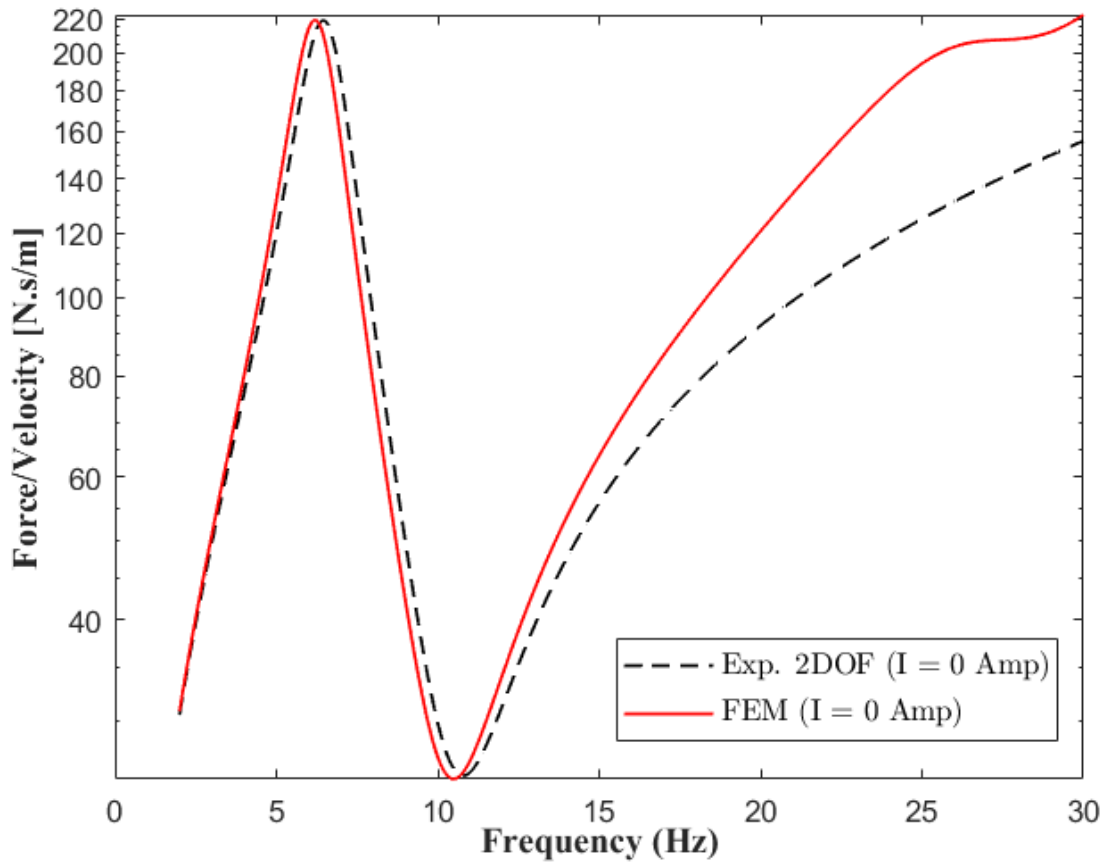
Figure 4.2 Point impedance of the equivalent model in the field-off state ($I = 0\ Amp$)

As it can be realized, the driving impedance point in the developed lumped model based on the experimental results reasonably agree with that derived using FE model particularly at operating low-frequency range. Moreover, results provided in Table 4.1 suggest that the change due to applied current in the optimum value of the masses of the equivalent lumped system is negligible. Therefore, the masses of the equivalent lumped model can be considered constant and the change in the natural frequency can be mainly attributed to the change in the equivalent stiffness.

4.3 Vibration Characterization of the System

The vibration absorber under study can be effectively used to attenuate the unwanted vibration of different structures. In particular it may be used to suppress the vibrations of

continuous structures such as structural cantilever beams. The continuous host structures may well be represented by an equivalent single degree of freedom model. The host structure and its equivalent model and parameters are shown in figure 4.3.
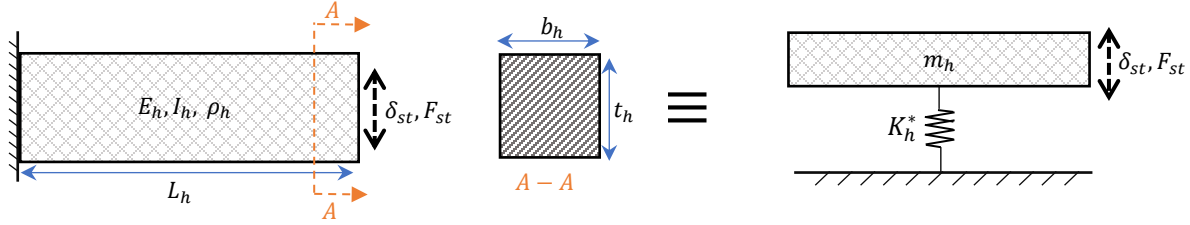
Figure 4.3 A beam-like host structural and equivalent model

As shown, m_h and K_h^* represent the equivalent sprung mass and complex stiffness of the structure, respectively. Also, the original host structure may be characterized by its length L_h, thickness t_h, width b_h, mass density ρ_h and young modulus E_h. Based on the analytical fundamental natural frequency and tip deflection δ_{st} of the beam-like host structure under static force F_{st}, the parameters for the equivalent model can be derived as follows:

$$m_h = \frac{K_h}{\omega_{h1}^2} \; ; \; K_h^* = K_h(1 + i\eta_h)$$
$$K_h = \frac{F_{st}}{\delta_{st}} \tag{4.6}$$

Where ω_{h1}, K_h and η_h represent the fundamental angular natural frequency, storage modulus and loss factor of the original host structure. The primary angular natural frequency and the tip deflection of the cantilever beam can be analytically derived as:

$$\delta_{st} = \frac{F_{st}L_h^3}{3E_hI_h}; \; \omega_{h1} \cong (1.875)^2 \sqrt{\frac{E_hI_h}{\rho_hA_hL_h^4}}$$
$$A_h = b_ht_h, I_h = \frac{1}{12}b_ht_h^3 \tag{4.7}$$

Thus, combining the two sets of Eq. (4.6) and Eq. (4.7), the equivalent parameters of the host structure may be obtained as functions of original system parameters. The equivalent storage modulus and mass are as follows:

$$m_h \cong (0.243)(\rho_h b_h t_h L_h), \qquad K_h = \frac{E_h b_h t_h^3}{4 L_h^3} \tag{4.8}$$

It should be noted that according to the formulation in Eq. (4.8), the sprung mass of the equivalent lumped model of the host structure comprises 0.243 of the overall cantilever beam structure. The host structure integrated with the SATVA and its lumped mass model can thus be shown as figure 4.4.
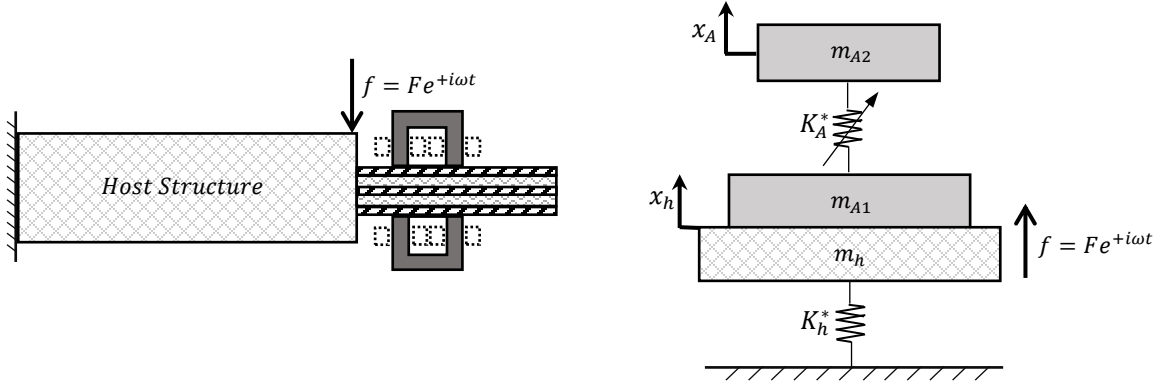
Figure 4.4 The overall structural assembly and equivalent model

As shown in figure 4.4, an external harmonic excitation force f with the excitation frequency of ω is applied to the host structure. The displacements x_A and x_h represent the displacements of the sprung mass of absorber and the host structure, respectively.

The governing equations of motion for the system can be written in the time domain as follows:

$$\begin{cases} m_{A2}\ddot{x}_A + \dfrac{K_A \eta_A}{\omega}(\dot{x}_A - \dot{x}_h) + K_A(x_A - x_h) = 0 \\[2mm] (m_{A1} + m_h)\ddot{x}_h + \dfrac{K_A \eta_A}{\omega}(\dot{x}_h - \dot{x}_A) + \dfrac{K_h \eta_h}{\omega}\dot{x}_h + K_A(x_h - x_A) + K_h x_h = f(t) \end{cases} \tag{4.9}$$

Utilizing the phasor representation for the displacements, the governing set of equations could be simplified in the frequency domain as follows:

$$\begin{cases} (K_A^* - \omega^2 m_{A2})X_A - K_A^* X_h = 0 \\ [K_h^* + K_A^* - \omega^2(m_{A1} + m_h)]X_h - K_A^* X_A = F \end{cases} \tag{4.10}$$

where F, X_A and X_h represent the Fourier transforms of excitation force, displacements x_A and x_h, respectively. From the equation (4.10), the steady-state amplitude, X_h can be derived as:

$$X_h = \cfrac{F}{\left[K_h^* + K_A^* - \omega^2(m_{A1} + m_h) - \cfrac{K_A^*}{\left(1 - \cfrac{\omega^2 m_{A2}}{K_A^*}\right)} \right]} \tag{4.11}$$

As it can be realized by tuning the natural frequency of the absorber that of the excitation frequency, $K_A = \omega^2 m_{A2}$, the host displacement amplitude can be minimized.

Therefore, a control law should be established to regulate the applied current to change the natural frequency of the absorber effectively to track the changing excitation frequency.

4.4 Adaptive phase-based Control law

In order to track the excitation frequency, an adaptive control law has been developed. First, the fundamentals of the Adaptive Kalman Filtering for full-state observation of a dynamic observable and controllable system are stated with the recursive Sage-Husa noise estimation techniques. Then, the control-law is established with derivation of state-space model of the system and the stiffness tuning algorithm formulated for the developed lumped dynamic system using the full-states observed by the adaptive Kalman Filter.

4.4.1 Full-State Observation using Adaptive Kalman Filter (AKF)

In this section, based on the Linear Minimum Variance Unbiased (LMVU) estimation of time-discrete systems, an Adaptive Kalman Filter (AKF) is formulated. First, the background information related to the estimation processes is provided and then the assumptions for the development of the adaptive estimator are stated. Next, the optimal parameters for various sections of the AKF were derived. Finally, the Sage-Husa recursive measurement noise and disturbance estimation method is discussed.

4.4.1.1 Background and Assumptions

The adaptive prediction filters deal with the continual estimation of parameters in a dynamic system, whose values change over time. The recursive updates used in the filters are based on sets of observations and measurements which contain information on the subgroups of the signal of interest (system states). The LMVU estimation techniques utilize the probability properties of changing signals, which include the Expected value, Variance and Covariance.

The expected value $\mathbb{E}[X]$ is defined as the weighted average or the arithmetic mean of a random variable X with independent realizations which is defined as follows:

$$X \text{ is a discreet variable} \implies \mathbb{E}[X] = \sum_{i=1}^{k} x_i p_i$$

$$X \text{ is a continuous variable} \implies \mathbb{E}[X] = \int_{\mathbb{R}} x f(x) dx \tag{4.12}$$

Where x_i and p_i represent the finite outcomes and their probability, respectively for the case of the expected value of a discreet variable. However, for the case of a continuous variable, the expected value could be determined using the probability density function $f(x)$ integrated over the whole domain of outcomes.

The covariance of two jointly distributed random variables X and Y, which measures the joint variability of the variables is defined as follows:

$$\text{COV}(X, Y) = \mathbb{E}[(X - \mathbb{E}[X])(Y - \mathbb{E}[Y])] \tag{4.13}$$

The variance of a random variable X is the expected value of the squared deviation of deviation from the arithmetic mean;

$$\text{Var}(X) = \text{COV}(X, X) = \mathbb{E}[(X - \mathbb{E}[X])^2] \tag{4.14}$$

The unbiased condition for the LMVU estimation requires the expectation of the output $\hat{x}$ of the estimator equals that of the original variable x ;

$$\mathbb{E}[\hat{x}] = \mathbb{E}[x] \tag{4.15}$$

Under the optimal LMVU estimators, the best estimate is achieved when the error variance at each time-step k is minimized as;

$$\hat{x}_k = \arg\min_{\hat{x}_k} \mathbb{E}[\|x_k - \hat{x}_k\|^2] = \mathbb{E}[(x_k - \hat{x}_k)^T(x_k - \hat{x}_k)] \tag{4.16}$$

The Kalman Filter is an LMVU estimator which offers the optimal performance in the class of linear filters on the dynamic time-varying systems.

As for the case under study, a real dynamic system may be modeled using the standard time-discrete state-space models augmented with noises and disturbance signals as follows:

$$\begin{cases} \underline{X}_{k+1} = \underline{\underline{\phi}}_{k+1,k}\underline{X}_k + \underline{\underline{\psi}}_{k+1,k}\underline{u}_k + \underline{\underline{\Gamma}}_{k+1,k}\underline{F}_k \\ \underline{Y}_{k+1} = \underline{\underline{H}}_{k+1}\underline{X}_{k+1} + \underline{v}_{k+1} \end{cases} \tag{4.17}$$

Where $\underline{X}_k$, $\underline{u}_k$ and $\underline{F}_k$ represent the full system state, the system input and the process noise (disturbance) at time-step k, respectively, while $\underline{\underline{\phi}}_{k+1,k}$, $\underline{\underline{\psi}}_{k+1,k}$ and $\underline{\underline{\Gamma}}_{k+1,k}$ represent the state, input and disturbance transition matrices between consecutive time-steps. Also $\underline{Y}_{k+1}$, $\underline{\underline{H}}_{k+1}$ and $\underline{v}_{k+1}$ represent the measurement (observation), observation matrix and the measurement noise signal, respectively.

Some assumptions were made before the derivation of the AKF full-state estimator. It is assumed that the measurement and process noise signals are uncorrelated and drawn from a natural gaussian distribution;

$$\mathbb{E}\left[\left(\underline{F}_k - \underline{q}_k\right)\left(\underline{F}_l - \underline{q}_l\right)^T\right] = \begin{cases} \underline{\underline{Q}}_k & ;k = l \\ 0 & ;k \neq l \end{cases}$$

$$\mathbb{E}\left[\left(\underline{v}_k - \underline{r}_k\right)\left(\underline{v}_l - \underline{r}_l\right)^T\right] = \begin{cases} \underline{\underline{R}}_k & ;k = l \\ 0 & ;k \neq l \end{cases}$$

$$\underline{F}_k \sim N(\underline{q}_k, \underline{\underline{Q}}_k), \qquad \underline{v}_k \sim N(\underline{r}_k, \underline{\underline{R}}_k) \tag{4.18}$$

Where $\underline{q}_k$, $\underline{\underline{Q}}_k$, $\underline{r}_k$ and $\underline{\underline{R}}_k$ denote the noise signal average, covariance, measurement noise average and covariance, respectively.

The initial system state $\underline{X}_0$ is considered a random signal uncorrelated to the system and noise processes with a known average $\hat{\underline{X}}_{0|0}$ and covariance matrix $\underline{P}_{0|0}$;

$$\hat{\underline{X}}_{0|0} = \mathbb{E}[\underline{X}_0], \qquad \underline{P}_{0|0} = \mathbb{E}\left[(\underline{X}_0 - \hat{\underline{X}}_{0|0})(\underline{X}_0 - \hat{\underline{X}}_{0|0})^T\right] \tag{4.19}$$

Provided the assumptions, based on sets of observations $\underline{Y}_1, \ldots, \underline{Y}_k$, the optimal Kalman Filter outputs the best estimate of the full state $\underline{X}_k$ (denoted as $\hat{\underline{X}}_k$) which corresponds to the minimization of error variance in Eq. (4.16).

4.4.1.2 Derivation of optimal operators of AKF

Considering the one-step-ahead prediction $\hat{\underline{X}}_{k+1|\underline{Y}^k}$ which is the estimation of the system state $\hat{\underline{X}}_{k+1}$ based on the sets of observations $\underline{Y}_1, \ldots, \underline{Y}_k$, we have the following:

$$\begin{aligned}
\hat{\underline{X}}_{k+1|k} &= \mathbb{E}\left[\underline{X}_{k+1}\,\middle|\,\underline{Y}_1, \ldots, \underline{Y}_k\right] \\
&= \mathbb{E}\left[\underline{\phi}_{k+1,k}\underline{X}_k + \underline{\psi}_{k+1,k}\underline{u}_k + \underline{\Gamma}_{k+1,k}\underline{F}_k\,\middle|\,\underline{Y}^k\right] \\
&= \underline{\phi}_{k+1,k}\mathbb{E}\left[\underline{X}_k\,\middle|\,\underline{Y}^k\right] + \underline{\psi}_{k+1,k}\underline{u}_k + \underline{\Gamma}_{k+1,k}\mathbb{E}\left[\underline{F}_k\,\middle|\,\underline{Y}^k\right] \\
&= \underline{\phi}_{k+1,k}\hat{\underline{X}}_{k|k} + \underline{\psi}_{k+1,k}\underline{u}_k + \underline{\Gamma}_{k+1,k}\hat{\underline{q}}_k
\end{aligned} \tag{4.20}$$

Where $\hat{\underline{X}}_{k|k}$ and $\hat{\underline{q}}_k$ indicate the estimate of the system state and process noise at time-step k based on the first k measurements.

Utilizing the state-space equation, Eq. (4.20) and the uncorrelation between $\hat{\underline{q}}_k$ and $\hat{\underline{X}}_{k|k}$ the estimate variance $\underline{P}_{k+1|k}$ for $\hat{\underline{X}}_{k+1|k}$ could be then derived as:

$$\begin{aligned}
\underline{P}_{k+1|k} &= \mathbb{E}\left[(\underline{X}_{k+1} - \hat{\underline{X}}_{k+1|k})(\underline{X}_{k+1} - \hat{\underline{X}}_{k+1|k})^T\,\middle|\,\underline{Y}^k\right] \\
&= \mathbb{E}\left[\left[\underline{\phi}_{k+1,k}(\underline{X}_k - \hat{\underline{X}}_{k|k}) + \underline{\Gamma}_{k+1,k}(\underline{F}_k - \hat{\underline{q}}_k)\right]\left[(\underline{X}_k - \hat{\underline{X}}_{k|k})^T\underline{\phi}_{k+1,k}^T + (\underline{F}_k - \hat{\underline{q}}_k)^T\underline{\Gamma}_{k+1,k}^T\right]\middle|\,\underline{Y}^k\right] \\
&= \underline{\phi}_{k+1,k}\mathbb{E}\left[(\underline{X}_k - \hat{\underline{X}}_{k|k})(\underline{X}_k - \hat{\underline{X}}_{k|k})^T\right]\underline{\phi}_{k+1,k}^T + \underline{\Gamma}_{k+1,k}\mathbb{E}\left[(\underline{F}_k - \hat{\underline{q}}_k)(\underline{F}_k - \hat{\underline{q}}_k)^T\right]\underline{\Gamma}_{k+1,k}^T \\
&= \underline{\phi}_{k+1,k}\underline{P}_{k|k}\underline{\phi}_{k+1,k}^T + \underline{\Gamma}_{k+1,k}\underline{Q}_k\underline{\Gamma}_{k+1,k}^T
\end{aligned} \tag{4.21}$$

51

Taking into account a new observation $\underline{Y}_{k+1}$ the previous state estimate $\underline{\hat{X}}_{k+1|k}$ can be updated to predict $\underline{\hat{X}}_{k+1|k+1}$ with a linear transform;

$$\underline{\hat{X}}_{k+1|k+1} = \underline{K}'_{k+1} \, \underline{\hat{X}}_{k+1|k} + \underline{K}_{k+1}\underline{Y}_{k+1} \tag{4.22}$$

To find the optimal gain matrices $\underline{K}'_{k+1}$ and $\underline{K}_{k+1}$, the unbiased condition is used along with the minimization of the error variance in Eq. (4.16).

Assuming that $\underline{\hat{X}}_{k|k}$ and $\hat{q}_k$ are unbiased, according to Eq. (4.20) the following could be established:

$$\mathbb{E}\left[\underline{\hat{X}}_{k+1|k}\right] = \underline{\phi}_{k+1,k}\mathbb{E}\left[\underline{\hat{X}}_{k|k}\right] + \underline{\psi}_{k+1,k}\underline{u}_k + \underline{\Gamma}_{k+1,k}\mathbb{E}\left[\hat{q}_k\right]$$

$$= \mathbb{E}\left[\underline{X}_{k+1}\right] \tag{4.23}$$

The unbiased condition further requires $\mathbb{E}\left[\underline{\hat{X}}_{k+1|k+1}\right] = \mathbb{E}\left[\underline{X}_{k+1}\right]$, utilizing the state-space relation and Eq. (4.22) and (4.23), the one-step-ahead unbiased relation results in the following;

$$\mathbb{E}\left[\underline{\hat{X}}_{k+1|k+1}\right] = \mathbb{E}\left[\underline{K}'_{k+1} \, \underline{\hat{X}}_{k+1|k} + \underline{K}_{k+1}\left[\underline{H}_{k+1}\underline{X}_{k+1} + \underline{v}_{k+1}\right]\right]$$

$$= \underline{K}'_{k+1}\mathbb{E}\left[\underline{\hat{X}}_{k+1|k}\right] + \underline{K}_{k+1}\underline{H}_{k+1}\mathbb{E}\left[\underline{X}_{k+1}\right] + \underline{K}_{k+1}\mathbb{E}\left[\underline{v}_{k+1}\right]$$

$$= \left[\underline{K}'_{k+1} + \underline{K}_{k+1}\underline{H}_{k+1}\right]\mathbb{E}\left[\underline{\hat{X}}_{k+1|k}\right] + \underline{K}_{k+1}\hat{r}_{k+1}$$

$$\mathbb{E}\left[\underline{\hat{X}}_{k+1|k+1}\right] = \mathbb{E}\left[\underline{\hat{X}}_{k+1|k}\right] \Rightarrow \underline{K}'_{k+1} = I - \underline{K}_{k+1}\underline{H}_{k+1} - \underline{K}_{k+1}\hat{r}_{k+1}\left(\mathbb{E}\left[\underline{\hat{X}}_{k+1|k}\right]\right)^{-1} \tag{4.24}$$

Combining the Eq. (4.24) for $\underline{K}'_{k+1}$ and the Eq. (4.22), the updated prediction can be calculated as:

$$\underline{\hat{X}}_{k+1|k+1} = \underline{\hat{X}}_{k+1|k} + \underline{K}_{k+1}\left[\underline{Y}_{k+1} - \left[\underline{H}_{k+1}\underline{\hat{X}}_{k+1|k} + \hat{r}_{k+1}\underbrace{\left(\mathbb{E}\left[\underline{\hat{X}}_{k+1|k}\right]\right)^{-1}\underline{\hat{X}}_{k+1|k}}_{I}\right]\right]$$

$$= \underline{\hat{X}}_{k+1|k} + \underline{K}_{k+1}\left[\underline{Y}_{k+1} - \underbrace{\left[\underline{H}_{k+1}\underline{\hat{X}}_{k+1|k} + \hat{r}_{k+1}\right]}_{\underline{\hat{Y}}_{k+1|k}}\right]$$

$$= \underline{\hat{X}}_{k+1|k} + \underline{K}_{k+1}\left[\underline{v}_{k+1}\right] \tag{4.25}$$

It should be noted that the matrix $\underline{K}_{k+1}$ is referred to as the Kalman gain.

Then utilizing Eq. (4.25) and the estimation error as $\underline{\tilde{X}}_{k+1|k} = \underline{\hat{X}}_{k+1|k} - \underline{X}_{k+1}$, the updated error covariance could be derived, as follows:

$$
\begin{aligned}
\underline{P}_{k+1|k+1} &= \mathbb{E}\left[\left(\underline{X}_{k+1} - \underline{\hat{X}}_{k+1|k+1}\right)\left(\underline{X}_{k+1} - \underline{\hat{X}}_{k+1|k+1}\right)^T \middle| \underline{Y}^{k+1}\right] \\
&= \mathbb{E}\left[\left[\left(\underline{K}_{k+1}\underline{H}_{k+1} - I\right)\underline{\tilde{X}}_{k+1|k} - \underline{K}_{k+1}(\underline{v}_{k+1} - \hat{r}_{k+1})\right]\left[\left(\underline{K}_{k+1}\underline{H}_{k+1} - I\right)\underline{\tilde{X}}_{k+1|k} - \underline{K}_{k+1}(\underline{v}_{k+1} - \hat{r}_{k+1})\right]^T\right] \\
&= \left(\underline{K}_{k+1}\underline{H}_{k+1} - I\right)\mathbb{E}[\underline{\tilde{X}}_{k+1|k}\underline{\tilde{X}}_{k+1|k}^T]\left(\underline{K}_{k+1}\underline{H}_{k+1} - I\right)^T + \underline{K}_{k+1}\mathbb{E}\left[(\underline{v}_{k+1} - \hat{r}_{k+1})(\underline{v}_{k+1} - \hat{r}_{k+1})^T\right]\underline{K}_{k+1}^T \\
&= \left(\underline{K}_{k+1}\underline{H}_{k+1} - I\right)\underline{P}_{k+1|k}\left(\underline{K}_{k+1}\underline{H}_{k+1} - I\right)^T + \underline{K}_{k+1}\underline{\widehat{R}}_{k+1}\underline{K}_{k+1}^T \qquad (4.26)
\end{aligned}
$$

The optimal gain for the Kalman filter, can then be derived by minimization of the error variance which corresponds to minimization of the trace of covariance matrix $\underline{P}_{k+1|k}$;

$$
\frac{\partial}{\partial \underline{K}_{k+1}}\left(\text{tr}(\underline{P}_{k+1|k+1})\right) = 0 \Rightarrow 2\left(\underline{K}_{k+1}\underline{H}_{k+1} - I\right)\underline{P}_{k+1|k}\underline{H}_{k+1}^T + 2\underline{K}_{k+1}\underline{\widehat{R}}_{k+1} = 0
$$

$$
\underline{K}_{k+1} = \underline{P}_{k+1|k}\underline{H}_{k+1}^T\left[\underline{H}_{k+1}\underline{P}_{k+1|k}\underline{H}_{k+1}^T + \underline{\widehat{R}}_{k+1}\right]^{-1} \qquad (4.27)
$$

The combination of Eq. (4.27) and (4.25), leads to the optimal linear filter known as the Kalman Filter.

It should also be noted that under the optimal $\underline{K}_{k+1}$ gain matrix, the updated error covariance can be simplified into the following:

$$
\underline{P}_{k+1|k+1} = \left(I - \underline{K}_{k+1}\underline{H}_{k+1}\right)\underline{P}_{k+1|k} \qquad (4.28)
$$

The schematic of a discretized Kalman Filter in each step is summarized in a flowchart shown in figure 4.5.
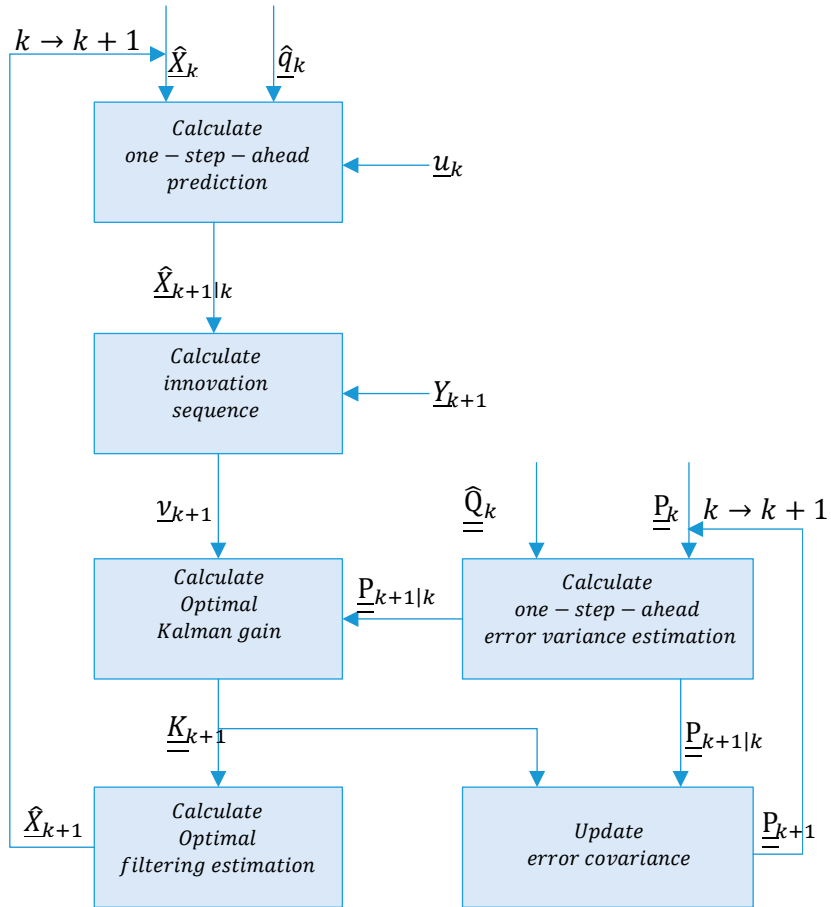
Figure 4.5 Schematic of discretized Kalman filter at step k

It should be noted that the noise variance $\widehat{\underline{\underline{Q}}}_k$ and average $\widehat{\underline{q}}_k$ are updated and fed to the Kalman Filter from the recursive estimator.

4.4.1.3 Sage-Husa measurement and process noise estimation

The traditional Kalman Filter estimation techniques require the exact mean and covariance for the measurement and process noise to operate optimally. To compensate for ongoing changes in the working/loading conditions of a vibration absorber, it is difficult to model the measurement and process noise. The Sage-Husa methods could be benefited to provide real-time estimations for the measurement and process noise signal properties, which are based on recursive modelling.

To further simplify the models, two parameters are introduced as follows:

$$G = \left[\underline{\Gamma}_{k+1,k}^T \underline{\Gamma}_{k+1,k}\right]^{-1} \underline{\Gamma}_{k+1,k}^T$$

$$d_k = \frac{1 - b_{SH}}{1 - b_{SH}^{k+1}}, \qquad 0 < b_{SH} < 1 \tag{4.29}$$

Where b_{SH} represents the forgetting factor. Based on the works of Andrew P. Sage and Gary W. Husa on algorithms for sequential adaptive estimation [52], the updated measurement and process noise signals' average and error variance in the time-step $k + 1$ may be derived from time-step k as:

$$\underline{F}_k : \begin{cases} \hat{\underline{q}}_{k+1} = (1 - d_k)\hat{\underline{q}}_k + d_k G\left(\hat{\underline{X}}_{k+1} - \underline{\phi}_{k+1,k}\hat{\underline{X}}_k\right) \\ \hat{\underline{Q}}_{k+1} = (1 - d_k)\hat{\underline{Q}}_k + d_k \left[G\left(\underline{K}_{k+1}\underline{v}_{k+1}\underline{v}_{k+1}^T\underline{K}_{k+1}^T + \underline{P}_{k+1} - \underline{\phi}_{k+1,k}\underline{P}_k\underline{\phi}_{k+1,k}^T\right)G^T\right] \end{cases}$$

$$\underline{v}_k : \begin{cases} \hat{\underline{r}}_{k+1} = (1 - d_k)\hat{\underline{r}}_k + d_k \left(\underline{Y}_{k+1} - \underline{H}_{k+1}\hat{\underline{X}}_{k+1|k}\right) \\ \hat{\underline{R}}_{k+1} = (1 - d_k)\hat{\underline{R}}_k + d_k \left(\underline{v}_{k+1}\underline{v}_{k+1}^T - \underline{H}_{k+1}\underline{P}_{k+1|k}\underline{H}_{k+1}^T\right) \end{cases} \tag{4.30}$$

4.4.2 Development of the control law

4.4.2.1 State-Space representation of the system

Since the considered vibration absorber works in the low-frequency range and with the assumption that the changes in excitation frequency are not abrupt, the structural damping can be represented by viscous damping in the equivalent model as in figure 4.6.
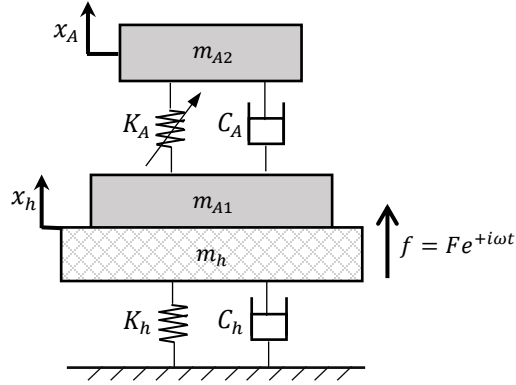
Figure 4.6 The overall simplified assembly with viscous damping

In the vicinity of their natural frequencies, the relationship between the damping ratio ξ_A, ξ_h and the loss factor, η_A, η_h for the host structure and the vibration absorber can be approximated as:

$$\xi_A = \frac{\eta_A}{2}, \quad \xi_h = \frac{\eta_h}{2} \tag{4.31}$$

The damping coefficients may then be represented as:

$$C_A = 2\xi_A m_{A2}\omega_A, \qquad C_h = 2\xi_h m_h \omega_h \tag{4.32}$$

The dynamic system state vector may be defined as:

$$\underline{X}(t) = \begin{bmatrix} x_A \\ \dot{x}_A \\ x_h \\ \dot{x}_h \end{bmatrix}$$

Then the time derivative of the state vector may be represented as:

$$\underline{\dot{X}}(t) = \begin{bmatrix} \dot{x}_A \\ \ddot{x}_A \\ \dot{x}_h \\ \ddot{x}_h \end{bmatrix}$$

$$= \begin{bmatrix} X(2) \\ \left[C_A\big(X(4) - X(2)\big) + K_A\big(X(3) - X(1)\big)\right]\dfrac{1}{m_{A2}} \\ X(4) \\ \dfrac{1}{m_{A1} + m_h}[K_A X(1) - (K_A + K_h)X(3) + C_A X(2) - (C_A + C_h)X(4)] + \dfrac{f(t)}{m_{A1} + m_h} \end{bmatrix}$$

The State-Space representation of the overall assembly may be simplified by defining some parameters as follows:

$$\left. \begin{array}{l} K_A = m_{A2}\omega_A^2 \\ K_{A0} = m_{A2}\omega_{A0}^2 \end{array} \right\} \Rightarrow K_A = K_{A0} + m_{A2}(\omega_A^2 - \omega_{A0}^2), \quad u(t) = (m_{A2}\omega_A^2 - K_{A0})(x_A - x_h) \qquad (4.34)$$

Where K_{A0} and ω_{A0} represent the idling stiffness and natural frequency of the vibration absorber which correspond to the off-state conditions of the absorber. Also, $u(t)$ represent the semi-active force of the vibration absorber.

Choosing the displacement of the host structure as the out-put feedback from the system, the continuous state-space representation of the system may then be formulated as follows:

$$\underline{\dot{X}}(t) = \underline{\underline{A}}\underline{X}(t) + \underline{B}_1 u(t) + \underline{B}_2 f(t)$$

$$\underline{Y}(t) = \underline{C}\underline{X}(t)$$

$$\underline{\underline{A}} = \begin{bmatrix} 0 & 1 & 0 & 0 \\ -\dfrac{K_{A0}}{m_{A2}} & -\dfrac{C_A}{m_{A2}} & \dfrac{K_{A0}}{m_{A2}} & \dfrac{C_A}{m_{A2}} \\ 0 & 0 & 0 & 1 \\ \dfrac{K_{A0}}{m_{A1} + m_h} & \dfrac{C_A}{m_{A1} + m_h} & -\dfrac{(K_{A0} + K_h)}{m_{A1} + m_h} & -\dfrac{(C_A + C_h)}{m_{A1} + m_h} \end{bmatrix}$$

$$\underline{B}_1 = \begin{bmatrix} 0 & -\dfrac{1}{m_{A2}} & 0 & \dfrac{1}{m_{A1} + m_h} \end{bmatrix}^T$$

$$\underline{B}_2 = \begin{bmatrix} 0 & 0 & 0 & \dfrac{1}{m_{A1} + m_h} \end{bmatrix}^T$$

$$\underline{C} = \begin{bmatrix} 0 & 0 & 1 & 0 \end{bmatrix} \qquad (4.35)$$

It is of paramount importance to verify the system's observability and controllability before development of the control law. The observability ensures that the state vector can be fully estimated based on the output vectors while controllability remarks the control over

the state vector based on the input to the system. Based on the rank criterion, the necessary and sufficient conditions for the controllability and observability of a linear time-invariant system is as follows:

$$Controllabilty \Rightarrow \text{rank} \begin{bmatrix} \underline{B_1} & \underline{A}\underline{B_1} & \dots & \underline{A}^{n-1}\underline{B_1} \end{bmatrix} = n$$

$$Observability \Rightarrow \text{rank} \begin{bmatrix} \underline{C}^T & \underline{A}^T\underline{C}^T & \dots & \left(\underline{A}^T\right)^{n-1}\underline{C}^T \end{bmatrix} = n \tag{4.36}$$

For the dynamic system under study $n = 4$ which represents the order of the system. Incorporation of the Eq. (4.35) into the rank criterion in Eq. (4.36), the observability and controllability of the system is verified.

In order for the Sage-Husa noise estimation methods to be incorporated into the control law, the state-space in Eq. (4.35) must be discretized into the format in Eq. (4.17). The system matrixes $\underline{\phi}_{k+1,k}$, $\underline{\psi}_{k+1,k}$, $\underline{\Gamma}_{k+1,k}$, $\underline{H}_{k+1}$ may be expressed as:

$$\underline{\phi}_{k+1,k} = e^{\underline{A}T_s}$$

$$\underline{\psi}_{k+1,k} = \underline{A}^{-1}\left(\underline{\phi}_{k+1,k} - I\right)\underline{B_1}$$

$$\underline{\Gamma}_{k+1,k} = \underline{A}^{-1}\left(\underline{\phi}_{k+1,k} - I\right)\underline{B_2}$$

$$\underline{H}_{k+1} = \underline{C} \tag{4.37}$$

Where T_s represents the sampling time of discretization. It should be noted that the excitation force $f(t)$ and the semi-active force $u(t)$ are expressed as the system noise and the system input in the discretized state-space formulation.

4.4.2.2 Stiffness tuning algorithm for the system

To simplify the control objective, the frequency ratio is defined as:

$$\Omega = \frac{\omega_A}{\omega} \tag{4.38}$$

where ω_A and ω represent the fundamental natural frequency of the absorber and the excitation frequency, respectively. The control objective is tune to the absorber frequency to that of expiation frequency ($\Omega = 1$). To acquire information on the normalized frequency (frequency ratio) and tracking performance, the phase difference between the displacement signals (x_A and x_h in Figure 4.6) can be utilized. Considering the relative displacement of the absorber with respect to the host system from the simplified model in figure 4.6, the following transfer function relation can be derived;

$$(X_A - X_h)/X_h = \left[\frac{(\Omega^2 - 1) - i(2\xi_A\Omega)}{\sqrt{(\Omega^2 - 1)^2 + (2\xi_A\Omega)^2}}\right] \tag{4.39}$$

where X_A and X_h represent the Fourier transform of the displacement signals of the absorber and the host structure. The cosine value of the phase difference ϕ between the relative displacement $X_A - X_h$ and host displacement X_h can also be stated as:

$$\cos\phi = \frac{\Omega^2 - 1}{\sqrt{(\Omega^2 - 1)^2 + (2\xi_A\Omega)^2}} \tag{4.40}$$

The cosine of the phase difference in Eq. (4.40) can be effectively used to develop a control law to change the electrical current to the wirings according to the sign of the cosine value of the phase difference. When $\Omega < 1$ (excitation frequency is more than the natural frequency of the absorber), $\cos\phi$ would be negative, thus the current to the electromagnets in the adaptive absorber should be increased to increase the stiffness of MREs and subsequently the natural frequency of the absorber. On the other hand, when $\Omega > 1$(excitation frequency is less than the natural frequency of the absorber), $\cos\phi$ would be positive. This means that the current should be decreased to reduce the natural frequency of the absorber. The goal is to reach to the ideal condition of $\Omega = 1$ which yields $\cos\phi = 0$. Thus by monitoring $\cos\phi$, an effective control strategy can be developed.

In the phase-based control law presented in this study, the objective is to change the external stimuli (magnetic flux or electric current) in order to minimize the error between the natural frequency of the absorber and the excitation frequency. As mentioned above, to track the excitation frequency, the natural frequency of the absorber should increase

for $\Omega < 1$ and decrease for $\Omega > 1$. Therefore, the following relation may be established between the change in the electric current and the phase difference with a negative gain value γ:

$$\frac{dI}{dt} = \gamma \cos \phi \tag{4.41}$$

To derive the phase difference between two harmonic measured signals such as $x_1 = X_1 \sin(\omega t)$ and $x_2 = X_2 \sin(\omega t - \phi)$, Liao et. al [53] proposed a practical phase detection module in real time. For the phase detection, first the RMS values for these signals are calculated using a low-pass filter as:

$$x_i^2 = \frac{X_i^2}{2} - \frac{X_i^2}{2} \cos(2\omega t + 2\phi) \xrightarrow{Low-pass\ filter} Output = x_{i\ rms}^2 = \frac{X_i^2}{2} \tag{4.42}$$

The RMS values are then used to calculate the phase difference between the signals as below:

$$A = \frac{x_1 x_2}{x_{1rms} x_{2rms}} = \cos \phi - \cos(2\omega t - \phi) \xrightarrow{Low-pass\ filter} Output = \cos \phi \tag{4.43}$$

The schematic of the final proposed control strategy is depicted in block diagram shown in figure 4.7.
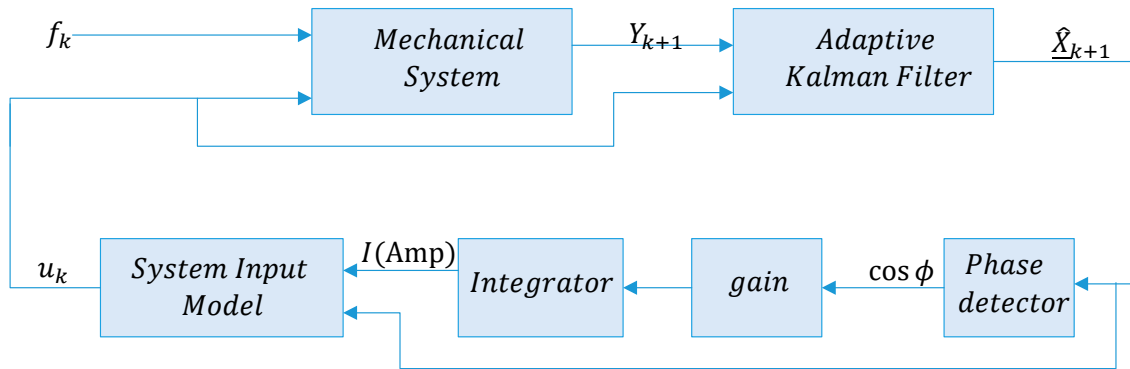

Figure 4.7 Schematic of the Control law

4.5 Results and Discussion

A cantilever beam-shape structure was chosen as the host system. The beam geometrical parameters and material property are defined as:

$$L_h = 200 \text{ cm}, b_h = 20 \text{ cm}, t_h = 3.45 \text{ cm}, \rho_h = 2710 \text{ kg/m}^3, E_h = 69 \text{ GPa} \qquad (4.44)$$

For practical consideration, it is important to verify the maximum induced bending stress and static tip deflection of the host structure under the total weight of the absorber:

$$\sigma_h = 1.136 \text{ MPa}, \delta_{st} = 1.3 \text{ mm} \qquad (4.45)$$

The static tip deflection of the host structure is well within the geometrical linearity region which can be approximated to 10% of the total beam length. Also, the maximum axial stress induced in the aluminum structure is well under the yield stress of the aluminum material (95 Mpa).

Considering the parameters in Eq (4.44) and considering a damping ratio of 5% for the fundamental mode, the following equivalent parameters are derived using eq. (4.8) for the host structure:

$$m_h \cong 9.09 \text{ } kg, K_h = 17.7 \text{ } kN/m, \xi_h = 0.05 \qquad (4.46)$$

Parameters for the adaptive SATVA were discussed in section 4.2 and table 4.1. In order to investigate the performance of the proposed phase-based control law, a harmonic excitation with varying frequency in the tunable range of SATVA is considered. The harmonic excitation force is defined as:

$$f(t) = 10(m_h + m_{A1}) \sin \omega t \qquad (4.47)$$

The control parameters, including the initial values for the noise average and variance are given in the table 4.2.

Table 4.2 Control Parameters

Parameter	Value	Parameter	Value
γ	-4	$\hat{R}_0$	2×10^{-13}
$T_s(s)$	10^{-3}	$\underline{\underline{P_0}}$	$\underline{\underline{0}}$

b_{SH}	0.99	$\widehat{Q}_0$	$10(m_h + m_{A1})$
$\hat{r}_0$	0	$\hat{q}_0$	0

The effectiveness of the phase-based control law is investigated by comparing the changes in the excitation frequency and the natural frequency of the adaptive absorber. The tracking phenomena is investigated by variations in the excitation frequency over time. Therefore, step variations in the tunable range of absorber were considered for the excitation frequency. The tracking performance was investigated in a $50s$ time span. The excitation frequency along with the tunable natural frequency of the absorber are shown in figure 4.8.

 Examination of figure 4.8 reveals that the excitation frequency varies four times in the time span of interest. The natural frequency of the absorber can successfully track the excitation using the proposed phase-based control law. Displacement of the host structure under the phase-based controller is also compared with the results of a passive absorber. The results are shown and compared in figure 4.9.

As depicted in figure 4.9, the steady-state displacement of the host structure during the four periods of variations in excitation frequency is reduced using the phase-based control approach. The steady-state displacement amplitude of the host structure is reduced by approximately 5.51%, 20.2% and 36.6% in the first $(0 - 15s)$, second $(15 - 25s)$ and third $(25 - 40s)$ period of variations, respectively. The observer performance is also investigated by comparing the measured and estimated displacement signal of the vibration absorber in figure 4.10. As it can be realized, the estimated displacement signal of the absorber follows closely the measured signal with a narrow margin of error.

Also, the effect of the variation of controller gain on the performance of the controller to track the excitation frequency is investigated and results are shown in figure 4.11.Results show that transient time delay, to reach to steady state at each step variation, can be noticeably decreased by increasing the magnitude of the gain.
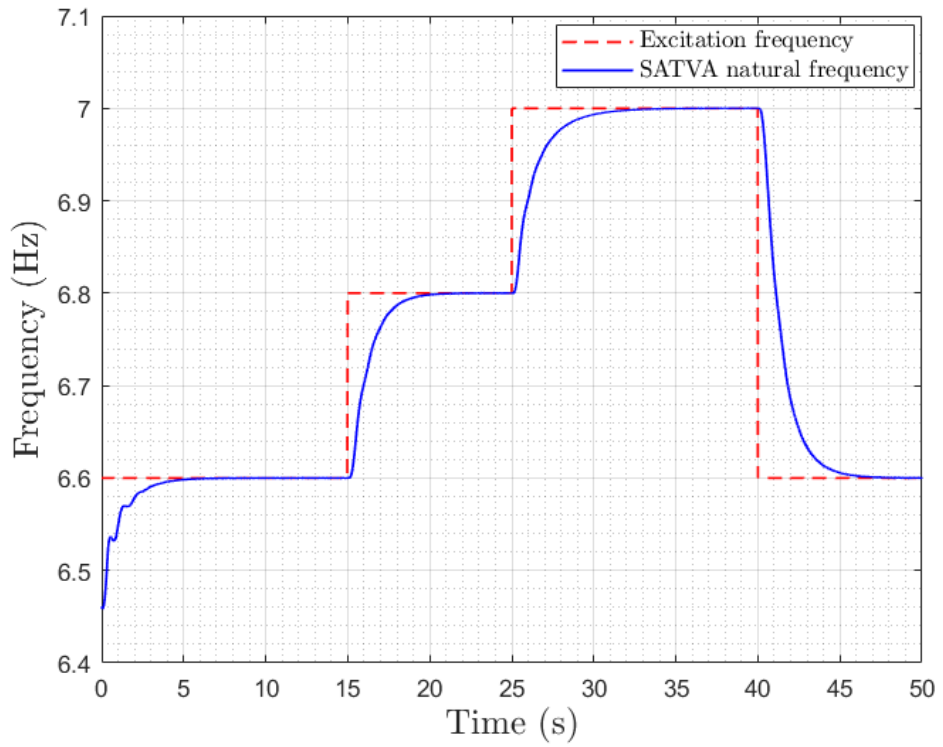
Figure 4.8 The variation in the excitation frequency vs the natural frequency variation
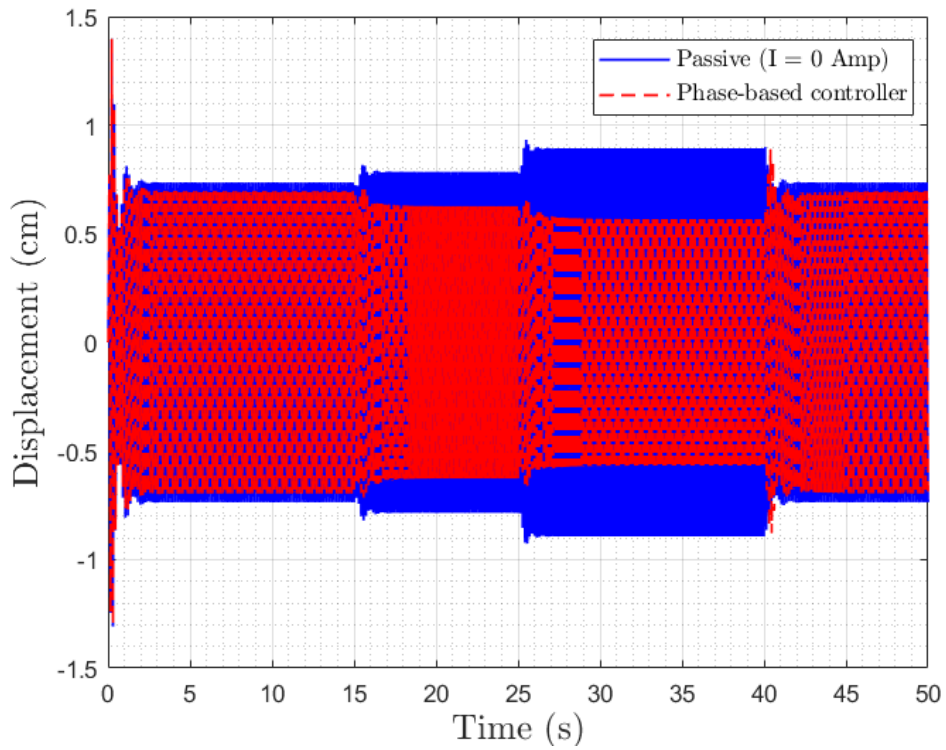

Figure 4.9 Displacement of the host structure
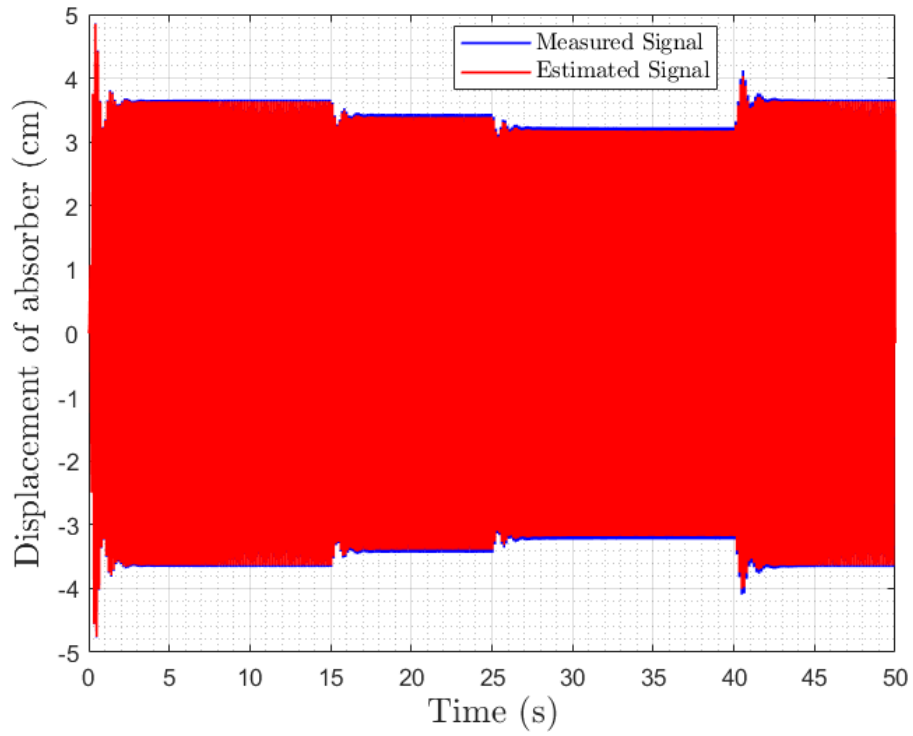
Figure 4.10 Measured vs Estimated displacement of vibration absorber
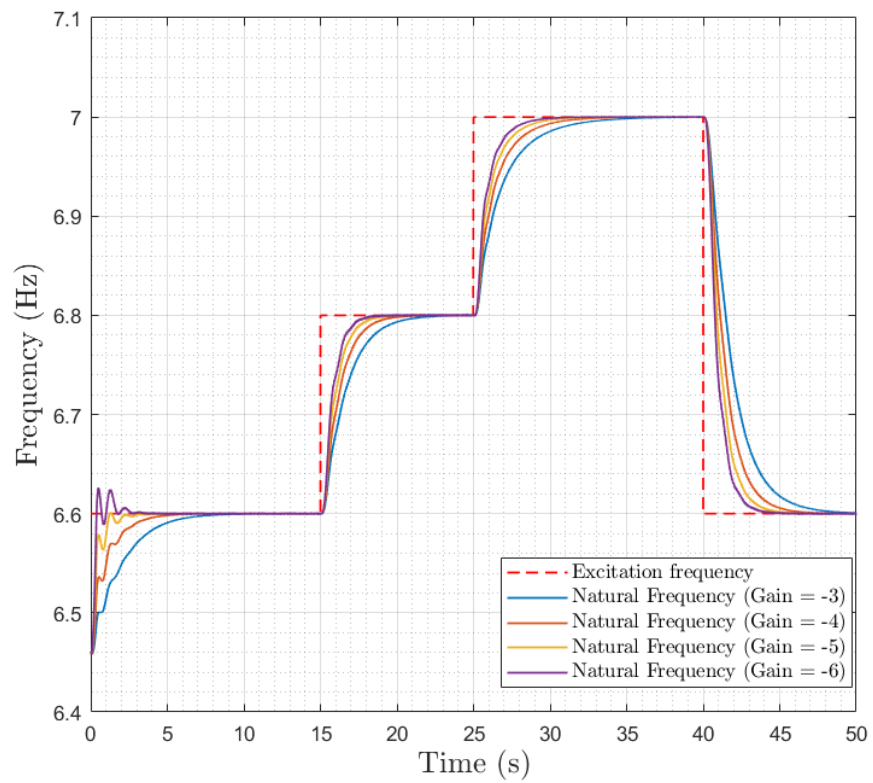
Figure 4.11 Natural Frequency variation with different controller gains

4.6 Conclusion

In this chapter, a practical phase-based control strategy is developed and investigated for vibration suppression of a host structure using the fabricated semi-active vibration absorber. First, a simplified lumped model for the vibration absorber was derived and characterized based on the experimental natural frequency values obtained under the open-loop experiments. Also, a beam-shape host structure was proposed and modeled as a single DOF system. The phase-based control law using adaptive Kalman filtering was subsequently developed. Finally, the performance of the developed control strategy was investigated and compared with the passive system.

Chapter 5: Contributions, Conclusions and Future Remarks

5.1 Major contributions

The main focus of this research study was to provide a comprehensive investigation into the design, development and adaptive control of a semi-active adaptive tunable vibration absorber featuring magnetorheological elastomers (MRE) sandwich beam. The MREs are a class of solid smart materials and composites that can provide variable stiffness compared with their magnetorheological fluid analogues. The key contributions of this thesis are the development, design, fabrication and adaptive control of a novel MRE-based sandwich structure as an adaptive vibration absorber. The contributions of this research are summarized as below:

i) Development of experiment-based finite element methods for analysis and design of the adaptive vibration absorber;

ii) Develop appropriate mechanical constraints and performance criteria for the design procedures of the vibration absorber;

iii) Fabricate the on-board electromagnets and the sandwich structure to validate the theoretical analysis;

iv) Formulation and development of an equivalent system based on the experimental open-loop tests;

v) Development of a practical, robust and adaptive control-law based on the use of Adaptive Kalman Filters (AKF) and the recursive Sage-Husa noise estimation techniques;

vi) The development, characterization alongside with the experimental results obtained from this dissertation have been published in the Smart Materials and Structures journal.

5.2 Major conclusions

This dissertation research presented appropriate design considerations, formulations and performance criteria of a novel semi-active adaptive tunable vibration absorber. Also, the development and formulation of an adaptive practical control-law was detailed and the results were compared with a passive absorber, to justify the benefit of the control-law. The major conclusions from this study are summarized as below:

(i) The developed Finite Element formulations for the sandwich structure can accurately be used to model the vibration absorber's frequency-shift and maximum stress in the layers resulted from the on-board electromagnets.

(ii) The developed Finite Element analysis of electromagnets can be used in conjunction with the experimental relative permeability of MRE samples to model the magnetic field density in the MRE layers of the vibration absorber.

(iii) The experimental rheological tests on the shear and loss modulus of MRE samples can be accurately used in the dynamic Finite Element formulations to predict the response of the adaptive vibration absorber to the electrical currents applied to the electromagnets' wirings.

(iv) An accurate lumped model can be developed from the experimental open-loop tests for the vibration absorber which proved to be accurate by comparing it against the previously verified Finite Element formulation.

(v) The Sage-Husa recursive noise estimation methods can be benefitted in the Adaptive Kalman Filters (AKFs), to optimally estimate the excitation frequency change and the full system state with the use of only one sensor, which reduces the implementational costs, and provides robustness in the practical applications.

5.3 Future remarks

While this research study has provided essential guidance for design and control of a MRE-sandwich beam based adaptive vibration absorber, there are still several issues that should be considered in future to improve the effectiveness of the absorber. These are summarized as follows:

(i) A multidisciplinary design optimization considering coupling between the magnetic circuit parameters, frequency-shift and mechanical constraints of absorber can provide a global optimum design parameter leading to lighter design with higher shift in the absorber's natural frequency.

(ii) The performance of the MRE-based adaptive vibration absorber to attenuate the vibration may be further improved by the incorporation of anisotropic MRE samples which suggest higher MR effects and higher relative permeability compared with isotropic MREs.

(iii) The temperature increase in the overall structure as a result of the electromagnets' wiring can result in the variation of moduli of MRE samples, which could be accounted for by incorporating the temperature-based models for MRE-samples.

(iv) The effectiveness of the proposed practical control-law should be further investigated by the implementation and hardware-in-the-loop (HIL) real-time simulations and experiments.

References

1.   Meirovitch, L., *Elements of Vibration Analysis, MacGraw Hill.* Inc., New York, NY, 1986: p. 290-296.
2.   Kim, H.K., H.S. Kim, and Y.-K. Kim, *Stiffness control of magnetorheological gels for adaptive tunable vibration absorber.* Smart Materials and Structures, 2016. **26**(1): p. 015016.
3.   Sun, S., et al., *An adaptive tuned vibration absorber based on multilayered MR elastomers.* Smart materials and structures, 2015. **24**(4): p. 045045.
4.   Susheelkumar, G., S. Murigendrappa, and K. Gangadharan, *Theoretical and experimental investigation of model-free adaptive fuzzy sliding mode control for MRE based adaptive tuned vibration absorber.* Smart Materials and Structures, 2019. **28**(4): p. 045017.
5.   Selvaraj, R. and M. Ramamoorthy, *Recent developments in semi-active control of magnetorheological materials-based sandwich structures: A review.* Journal of Thermoplastic Composite Materials, 2020: p. 0892705720930749.
6.   Abe, M. and T. Igusa, *Semi-active dynamic vibration absorbers for controlling transient response.* Journal of Sound and Vibration, 1996. **198**(5): p. 547-569.
7.   Jalili, N. and E. Esmailzadeh, *Adaptive-passive structural vibration attenuation using distributed absorbers.* Proceedings of the Institution of Mechanical Engineers, Part K: Journal of Multi-body Dynamics, 2002. **216**(3): p. 223-235.
8.   Franchek, M., M. Ryan, and R. Bernhard, *Adaptive passive vibration control.* Journal of Sound and Vibration, 1996. **189**(5): p. 565-585.
9.   Nagaya, K., et al., *Vibration control of a structure by using a tunable absorber and an optimal vibration absorber under auto-tuning control.* Journal of sound and vibration, 1999. **228**(4): p. 773-792.
10. Xu, Z., X. Gong, and X. Chen, *Development of a mechanical semi-active vibration absorber.* Advances in Vibration Engineering, 2011. **10**(3): p. 229-238.
11. Rustighi, E., M. Brennan, and B. Mace, *A shape memory alloy adaptive tuned vibration absorber: design and implementation.* Smart Materials and Structures, 2004. **14**(1): p. 19.
12. Gerlach, T., J. Ehrlich, and H. Böse. *Novel active vibration absorber with magnetorheological fluid.* in *Journal of Physics: Conference Series.* 2009. IOP Publishing.
13. Deng, H.-x., X.-l. Gong, and L.-h. Wang, *Development of an adaptive tuned vibration absorber with magnetorheological elastomer.* Smart materials and structures, 2006. **15**(5): p. N111.
14. Hollkamp, J.J. and T.F. Starchville Jr, *A self-tuning piezoelectric vibration absorber.* Journal of intelligent material systems and structures, 1994. **5**(4): p. 559-566.
15. Xin, F.-L., X.-X. Bai, and L.-J. Qian, *Principle, modeling, and control of a magnetorheological elastomer dynamic vibration absorber for powertrain mount systems of automobiles.* Journal of Intelligent Material Systems and Structures, 2017. **28**(16): p. 2239-2254.
16. Carlson, J.D. and M.R. Jolly, *MR fluid, foam and elastomer devices.* mechatronics, 2000. **10**(4-5): p. 555-569.
17. Rabinow, J., *The magnetic fluid clutch.* Electrical Engineering, 1948. **67**(12): p. 1167-1167.

18. Truong, D. and K. Ahn, *MR fluid damper and its application to force sensorless damping control system.* Smart Actuation and Sensing Systems-Recent Advances and Future Challenges, InTech, Rijeka, 2012: p. 383-424.

19. Ashtiani, M., S. Hashemabadi, and A. Ghaffari, *A review on the magnetorheological fluid preparation and stabilization.* Journal of magnetism and Magnetic Materials, 2015. **374**: p. 716-730.

20. Huang, J., et al., *Analysis and design of a cylindrical magneto-rheological fluid brake.* Journal of Materials Processing Technology, 2002. **129**(1-3): p. 559-562.

21. Lee, U., et al., *Design analysis and experimental evaluation of an MR fluid clutch.* Journal of Intelligent Material Systems and Structures, 1999. **10**(9): p. 701-707.

22. Spencer Jr, B.F., et al. *Smart dampers for seismic protection of structures: a full-scale study.* in *Proceedings of the second world conference on structural control.* 1998. Kyoto.

23. Lai, C.Y. and W.-H. Liao, *Vibration control of a suspension system via a magnetorheological fluid damper.* Journal of Vibration and Control, 2002. **8**(4): p. 527-547.

24. Bolat, F.C. and S. Sivrioglu, *Active vibration suppression of elastic blade structure: Using a novel magnetorheological layer patch.* Journal of Intelligent Material Systems and Structures, 2018. **29**(19): p. 3792-3803.

25. Sivrioglu, S. and F.C. Bolat, *Switching linear quadratic Gaussian control of a flexible blade structure containing magnetorheological fluid.* Transactions of the Institute of Measurement and Control, 2020. **42**(3): p. 618-627.

26. Shen, Y., M.F. Golnaraghi, and G.R. Heppler, *Experimental research and modeling of magnetorheological elastomers.* Journal of Intelligent Material Systems and Structures, 2004. **15**(1): p. 27-35.

27. Rigbi, Z. and L. Jilken, *The response of an elastomer filled with soft ferrite to mechanical and magnetic influences.* Journal of magnetism and magnetic materials, 1983. **37**(3): p. 267-276.

28. Liu, T. and Y. Xu, *Magnetorheological Elastomers: Materials and Applications*, in *Smart and Functional Soft Materials*. 2019, IntechOpen.

29. Gong, X., X. Zhang, and P. Zhang, *Fabrication and characterization of isotropic magnetorheological elastomers.* Polymer testing, 2005. **24**(5): p. 669-676.

30. Chen, L., X. Gong, and W. Li, *Microstructures and viscoelastic properties of anisotropic magnetorheological elastomers.* Smart Materials and Structures, 2007. **16**(6): p. 2645.

31. Li, W., X. Zhang, and H. Du, *Magnetorheological elastomers and their applications*, in *Advances in elastomers I*. 2013, Springer. p. 357-374.

32. Khanouki, M.A., R. Sedaghati, and M. Hemmatian, *Experimental characterization and microscale modeling of isotropic and anisotropic magnetorheological elastomers.* Composites Part B: Engineering, 2019. **176**: p. 107311.

33. Cantera, M.A., et al., *Modeling of magneto-mechanical response of magnetorheological elastomers (MRE) and MRE-based systems: a review.* Smart Materials and Structures, 2017. **26**(2): p. 023001.

34. Ahamed, R., S.-B. Choi, and M.M. Ferdaus, *A state of art on magneto-rheological materials and their potential applications.* Journal of Intelligent Material Systems and Structures, 2018. **29**(10): p. 2051-2095.

35. Sun, S., et al., *The development of an adaptive tuned magnetorheological elastomer absorber working in squeeze mode.* Smart Materials and Structures, 2014. **23**(7): p. 075009.

36. Lerner, A.A. and K. Cunefare, *Performance of MRE-based vibration absorbers.* Journal of Intelligent Material Systems and Structures, 2008. **19**(5): p. 551-563.

37. Ginder, J.M., W.F. Schlotter, and M.E. Nichols. *Magnetorheological elastomers in tunable vibration absorbers.* in *Smart structures and materials 2001: damping and isolation.* 2001. International Society for Optics and Photonics.

38. Deng, H.-x. and X.-l. Gong, *Application of magnetorheological elastomer to vibration absorber.* Communications in nonlinear science and numerical simulation, 2008. **13**(9): p. 1938-1947.

39. Dong, X.-M., et al., *A new variable stiffness absorber based on magneto-rheological elastomer.* Transactions of Nonferrous Metals Society of China, 2009. **19**: p. s611-s615.

40. Sun, S., et al., *Development of an MRE adaptive tuned vibration absorber with self-sensing capability.* Smart Materials and Structures, 2015. **24**(9): p. 095012.

41. Komatsuzaki, T., T. Inoue, and Y. Iwata, *Experimental investigation of an adaptively tuned dynamic absorber incorporating magnetorheological elastomer with self-sensing property.* Experimental Mechanics, 2016. **56**(5): p. 871-880.

42. Liu, G., et al., *Development of a semi-active dynamic vibration absorber for longitudinal vibration of propulsion shaft system based on magnetorheological elastomer.* Smart Materials and Structures, 2017. **26**(7): p. 075009.

43. Jang, D.I., et al., *Designing an attachable and power-efficient all-in-one module of a tunable vibration absorber based on magnetorheological elastomer.* Smart Materials and Structures, 2018. **27**(8): p. 085009.

44. Yang, J., et al., *Development and evaluation of an MRE-based absorber with two individually controllable natural frequencies.* Smart Materials and Structures, 2018. **27**(9): p. 095002.

45. Ammovilli, V., M. Bilasse, and I. Charpentier, *Continuous nonlinear eigenvalue solver with applications to the design of electro/magnetorheological sandwich structures.* Smart Materials and Structures, 2019. **28**(8): p. 085038.

46. DiTaranto, R., *Theory of vibratory bending for elastic and viscoelastic layered finite-length beams.* 1965.

47. DiTaranto, R. and W. Blasingame, *Composite damping of vibrating sandwich beams.* 1967.

48. Mead, D. and S. Markus, *The forced vibration of a three-layer, damped sandwich beam with arbitrary boundary conditions.* Journal of sound and vibration, 1969. **10**(2): p. 163-175.

49. Mead, D. and S. Markus, *Loss factors and resonant frequencies of encastre damped sandwich beams.* Journal of Sound and Vibration, 1970. **12**(1): p. 99-112.

50. Benaroya, H., M. Nagurka, and S. Han, *Mechanical vibration: analysis, uncertainties, and control.* 2017: CRC Press.

51. Meeker, D. *Finite Element Method Magnetics (Version 4.2).* FEMM 2010; Available from: www.femm.info.

52.   Sage, A.P. and G.W. Husa. *Algorithms for sequential adaptive estimation of prior statistics*. in *1969 IEEE Symposium on Adaptive Processes (8th) Decision and Control*. 1969. IEEE.

53.   Liao, G., X. Gong, and S. Xuan, *Phase based stiffness tuning algorithm for a magnetorheological elastomer dynamic vibration absorber.* Smart Materials and Structures, 2013. **23**(1): p. 015016.